The Astronomical Journal, 169:244 (18pp), 2025 May https://doi.org/10.3847/1538-3881/adbe6c

Photobombing for the Large Interferometer For Exoplanets (LIFE). A New Criterion for Target Confusion and Application to a Mid-infrared Rotating Nulling Interferometer

Drinor Cacaj[1,2], Daniel Angerhausen[1], Prabal Saxena[2], Romain Laugier[3], Jens Kammerer[4], Eleonora Alei[2], and Sascha P. Quanz[1,5]
[1] ETH Zurich, Institute for Particle Physics & Astrophysics, Wolfgang-Pauli-Str. 27, 8093 Zurich, Switzerland
[2] NASA Goddard Space Flight Center, Greenbelt, MD 20771, USA
[3] Institute of Astronomy, KU Leuven, Celestijnenlaan 200D, 3001, Leuven, Belgium
[4] European Southern Observatory, Karl-Schwarzschild-Straße 2, 85748 Garching, Germany
[5] ETH Zurich, Department of Earth Sciences, Sonneggstrasse 5, 8092 Zurich, Switzerland
Received 2024 October 21; revised 2025 February 27; accepted 2025 March 7; published 2025 April 3

Abstract

One of the primary objectives in modern astronomy is to discover and study planets with characteristics similar to Earth. This pursuit involves analyzing the spectra of exoplanets and searching for biosignatures. Contamination of spectra by nearby objects (e.g., other planets and moons in the same system) is a significant concern and must be addressed for future exo-Earth searching missions. The aim is to estimate, for habitable planets, the probability of spectral contamination by other planets within the same star system. This investigation focuses on the Large Interferometer For Exoplanets (LIFE). Since the Rayleigh criterion is inapplicable to interferometers such as those proposed for LIFE, we present new criteria based on the principle of parsimony that take into account two types of issues: contamination or blending of point sources and cancellation of point sources due to destructive interference. We define a new spatial resolution metric associated with contamination or cancellation that generalizes to a broader family of observing instruments. In the current baseline design, LIFE is an X-array architecture nulling interferometer. Our investigation reveals that its transmission map introduces the potential for two point sources to appear as one, even if they do not appear in close proximity. We find that LIFE has a spatial resolution comparable to that of a traditional telescope with a diameter of $D = 600$ m, observing at $\lambda = 4$ μm. Our survey of a star system population shows that, out of 73.4 expected habitable planets detected, 71.3 are not contaminated, on average.

Unified Astronomy Thesaurus concepts: Exoplanets (498); Habitable planets (695); Space telescopes (1547); Spectroscopy (1558); Interferometers (805)

1. Introduction

The Large Interferometer For Exoplanets (LIFE) is a space mission concept aimed at detecting and characterizing exoplanets in the habitable zone (HZ) of their host stars (S. P. Quanz et al. 2022). In its current design, LIFE is a nulling interferometer based on an X-array architecture with four collecting telescopes (Figure 1). It has two characteristic dimensions: the nulling baseline $b_{\rm null}$, which is adjustable from 10 m to 100 m, and the imaging baseline $b_{\rm im} = 6b_{\rm null}$. LIFE observes in the 4 μm–18.5 μm wavelength range. To make an observation, LIFE must rotate, and, unlike traditional telescopes, a monochromatic observation with LIFE will produce a time series instead of an image. A key concept to consider is its ability to resolve two point sources of light that may represent planets.

A first approach to estimate LIFE's spatial resolution is by comparing it to a traditional telescope of diameter equivalent to its imaging baseline. Following P. Saxena (2022), we refer to the terms "photobombing" contamination, or target confusion when two point sources representing planets satisfy a given contamination criterion. In P. Saxena (2022), the Rayleigh criterion was used to estimate spectral contamination. That criterion overestimates spectral contamination. It showed that, for future telescopes of size 6 m and 12 m observing in the near-IR, Earth would frequently get contaminated by other planets in the inner solar system, making biosignatures harder to detect. The aim of this paper is to quantify the spectral contamination occurrence for habitable planets by other planets within the same star system. Since the Rayleigh criterion is not applicable for nulling interferometers, we need to find a new contamination criterion that generalizes to traditional telescopes and interferometers like LIFE. This would allow us to compare the resolving capabilities of LIFE with traditional telescopes.

This paper contains key concepts related to the point-spread function (PSF) of a traditional telescope and its spatial resolution as defined by the Rayleigh criterion. Applying the principle of parsimony, we attempt to redefine and generalize the concept of spatial resolution by considering two issues that arise when using an observational instrument: the blending of two point sources into one and the potential for two point sources to cancel each other's signals while remaining detectable independently. The latter phenomenon does not affect traditional telescopes, but it does impact nulling interferometers. We then introduce new metrics denoted by δ_0 and δ_1 that quantify how much an observing instrument is susceptible to contamination and cancellation, respectively. First, we provide the δ_1 spatial resolution for a traditional telescope. In a second step, we examine how LIFE produces time series as images and give its associated δ_0 and δ_1 spatial resolution. The detection of habitable planets is quantified via the detection probability, which is the probability of a given planet being detected. The contamination of habitable planets is quantified via the contamination probability, which is the probability of a given detected planet

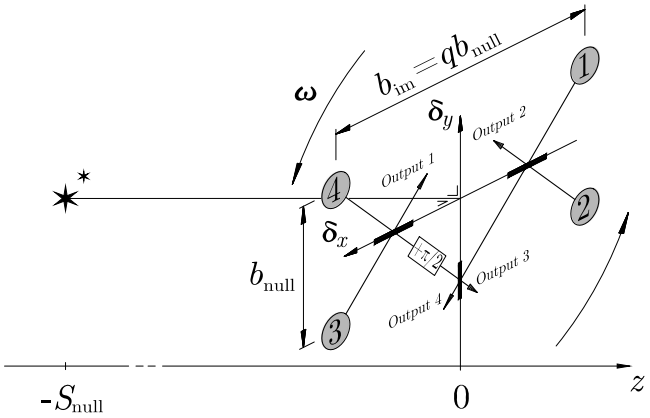

Figure 1. X-architecture rotating interferometer setup. The current LIFE design has a scaling factor of $q = 6$ and nulling baseline b_{null} that can be adjusted from 10 m to 100 m. For details about this setup, see S. P. Quanz et al. (2022).

being contaminated by another planet within the same stellar system. These quantities are calculated assuming that planets do not move during an observation. We briefly present numerical methods in Appendix A to estimate them for two point sources located in the field of view (FOV), each with its own spectrum.

Individual systems like the inner solar system and the TRAPPIST-1 system are examined. These systems provide two extreme-case scenarios for LIFE. The inner solar system can be directly compared with results from P. Saxena (2022). The detection and contamination probabilities will be provided for different values of the system's distance and inclination angle of the orbit plane, followed by a discussion of the results. After this stage, a population analysis study is conducted using the LIFEsim tool (F. A. Dannert et al. 2022) to estimate how much contamination we can expect during the search phase.

2. Theory

First, in Section 2.1, we briefly present the current definition of contamination, specifically the angular distance at which two point sources blend or become indistinguishable. In Section 2.2, we introduce a new criterion that is generalized for a broader range of observing instruments, accounting for both contamination and cancellation.

2.1. Spatial Resolution and Rayleigh Criterion

The PSF describes how a point source of light will appear behind a particular aperture (Figure 2). To simplify, we will consider a circular aperture and assume that the aperture is in the far field. For a monochromatic point source $p = ((\delta_{x,p} = 0, \delta_{y,p} = 0), F_p = 1)$, where $\delta_{x,p}$, $\delta_{y,p}$ is the position of the point source in the FOV and F_p is the incoming luminosity flux at wavelength λ, we get the well-known Airy disk function (F. R. S. Rayleigh 1879),

$$U_p(\delta_x, \delta_y, \lambda) = \left(\frac{2J_1(\pi\delta_r d/\lambda)}{\pi\delta_r d/\lambda}\right)^2, \qquad \delta_r = \sqrt{\delta_x^2 + \delta_y^2}, \quad (1)$$

where δ_x, δ_y are the angular separation in the x- and y-axes, respectively; λ is the wavelength; d is the diameter of the telescope; and J_1 is the Bessel function of the first kind of order 1. The first zero of $J_1(q)$ is at $q = q_0 \approx 3.8317$. The regular notion of spatial resolution is given by the Rayleigh criterion, which is defined by the angular separation to the first zero of the Airy disk,

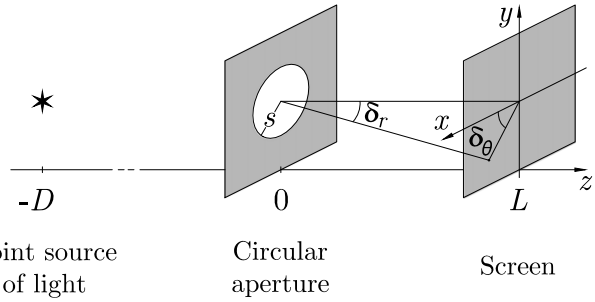

Figure 2. Conventional telescope setup with circular aperture. Far field approximation $D >> L$. Diameter $d = 2s$, where s is the radius of the circular aperture.

$$\pi\delta_{\text{Rayleigh}} d/\lambda = q_0 \quad \Rightarrow \quad \delta_{\text{Rayleigh}} \approx 1.22 \cdot \frac{\lambda}{d}. \quad (2)$$

For two monochromatic point sources of light, we say that photobombing/contamination occurs when the apparent angle between them is less than δ_{Rayleigh}.

In reality, we can resolve point sources even if their apparent angular separation is smaller than δ_{Rayleigh}, provided that we have a high enough signal-to-noise ratio (S/N). In theory, in the limit of high S/N, we can always resolve/deconvolute two point sources that do not have the same apparent position. Rayleigh's criterion focuses more on the potential for contamination rather than contamination in an absolute sense. A helpful interpretation is that Rayleigh's criterion intuitively tells us that if two point sources are separated by more than approximately δ_{Rayleigh}, regardless of the S/N, they cannot be mistaken for a single point source. This implies that if the amplitude of the background noise could be adjusted, the two point sources would fade into the noise before merging into one, as long as their angular separation exceeds δ_{Rayleigh}. It is arbitrarily defined using the first zero of the Airy disk and is therefore ill defined, making it difficult to generalize to other observing instruments.

2.2. Generalized Spectral Contamination Criterion

In this section, we construct a simple criterion to decide if spectral contamination occurs when observing planets within a star system. Assume the ground truth consists of two point sources representing two planets within a star system. The main idea used in this paper is to compare the best models against the ground truth, factoring in a parsimony cost that increases with the model's complexity. The parsimony cost allows us to select the best model with respect to the number of point sources. If the best model is a model with a single point source, then to validate spectral contamination, we add the following key condition: if the best single-point-source model does not resemble one of the ground truth's point sources, then contamination occurs. This ensures that the best model does not represent something that exists already. A similarity measure between outputs is necessary for comparisons. Outputs can be either image-like or time-series-like, depending on the type of telescope. We will use the Kullback–Leibler (KL) divergence (S. Kullback 1997) on Gaussian multivariate distributions, which represent the outputs of a given telescope and observed system factoring in the sources and background noise.

2.2.1. Photon Density Distributions

First, we define a point source of light p to be given by its apparent position and incoming photon flux over the wavelengths of observation $\hat{\Lambda} = \{\lambda_1, \ldots, \lambda_M\}$ defined by the wavelength range Λ and spectral resolution R:

$$p = (\boldsymbol{\theta}_p = (\delta_x, \delta_y), \boldsymbol{F}_p = (F_{p,\lambda_1}, \ldots, F_{p,\lambda_M})). \tag{3}$$

In this paper, a given set of point sources is also referred to as a configuration of point sources. They will represent planets located in the FOV.

We define the unit instrument response function (UIRF) U_p as the noiseless output of a telescope for a given point source $p = (\boldsymbol{\theta}_p, \boldsymbol{F}_p = \mathbf{1})$ with unit luminosity flux across $\lambda_1, \ldots, \lambda_M$. It can be image-like or time-series-like. Unlike the common PSF, it generally depends on the location $\boldsymbol{\theta}_p = (\delta_x, \delta_y)$ in the FOV. For example, for a circular-aperture telescope, the UIRFs are given by the Airy disk functions U_p (Equation (1)), centered at $(\delta_{x,p}, \delta_{y,p})$, i.e., $\delta_r = \sqrt{(\delta_x - \delta_{x,p})^2 + (\delta_y - \delta_{y,p})^2}$. U_p depends on geometrical hyperparameters. For example, the diameter d of the telescope would be one such parameter.

Given a point source $p = (\boldsymbol{\theta}_p, \boldsymbol{F}_p)$ and a background noise covariance matrix Σ, we define the monochromatic photon density distribution $\mathcal{N}_p(\lambda)$ as the following multivariate Gaussian distribution:

$$\mathcal{N}_p(\lambda) = \mathcal{N}(\boldsymbol{\mu}_p(\lambda), \Sigma(\lambda)), \quad \text{where} \quad \boldsymbol{\mu}_p(\lambda) = F_{p,\lambda}\boldsymbol{U}_p(\lambda), \tag{4}$$

where $\boldsymbol{U}_p = (U_{p,g_1,\ldots,g_k})_{(g_1,\ldots,g_k)\in\Gamma}$ is a column vector representing the UIRF of the considered telescope for a given point source p. $G = \{g_1, \ldots, g_K\}$ denotes the output parameters of that telescope. $G = \{\delta_x, \delta_y\}$ for traditional telescopes, and $G = \{\rho\}$ for LIFE, where ρ is the angle of rotation of LIFE. Γ denotes the output parameter space grid, which is assumed to be equally spaced. For instance, Γ can represent the grid of pixels, or it can represent the discrete set of angles of rotation of LIFE. $\mathcal{N}_P(\lambda)$ represents the distribution of monochromatic images given a single point source p factoring in a background noise via the covariance matrix Σ. In this study, we neglect pixel noise; i.e., we assume that the pixel size is small compared to the variation of the UIRF. Moreover, we assume that planet noise is negligible compared to the background noise. Thus, for configurations with multiple point sources $P = \{p_1, p_2\}$, we simply add the means $\boldsymbol{\mu}_p(\lambda)$ while keeping the same background noise, i.e., $\mu_P = \mu_{p_1} + \mu_{p_2}$ and $\Sigma_P = \Sigma_{p_1} = \Sigma_{p_2} = \Sigma$.

Unlike for traditional telescopes, the convolution idea with PSFs used in traditional telescopes does not work for LIFE. We notice that the shape of the time series $\boldsymbol{U}_p$ generally depends on the position of the point source p in the FOV. We will see that for LIFE, there is generally a different UIRF for different apparent positions of p in the FOV. To calculate the photon density distribution of a point source p for LIFE, i.e., a time series for a fixed wavelength, we "convolute" with a nonconstant "PSF," which in this case is the UIRF of LIFE, and calculate the background noise term using LIFEsim (F. A. Dannert et al. 2022).

2.2.2. The Cost Function

In this paper, we use the KL divergence D_{KL} to measure the similarity between two multivariate Gaussian distributions

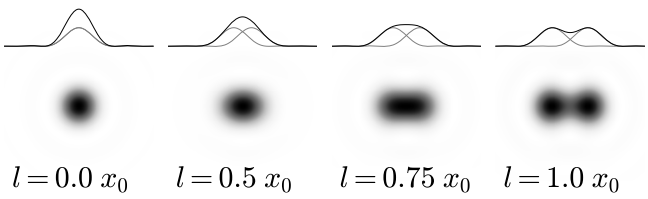

Figure 3. Screen outputs from two point sources of light with an apparent angular distance between them of l, where $x_0 = \delta_{\mathrm{Rayleigh}}$.

$\mathcal{N}_P(\lambda)$ and $\mathcal{N}_Q(\lambda)$ representing monochromatic outputs from point source P and Q, respectively. It has the following closed form solution (L. Pardo 2018):

$$\begin{aligned} & D_{\mathrm{KL}}(\mathcal{N}_P(\lambda) \| \mathcal{N}_Q(\lambda)) \\ &= \tfrac{1}{2}(\mathrm{tr}(\Sigma_Q^{-1}\Sigma_P) - K + (\boldsymbol{\mu}_Q - \boldsymbol{\mu}_P)^t \Sigma_Q^{-1}(\boldsymbol{\mu}_Q - \boldsymbol{\mu}_P) \\ &\quad + \ln\left(\tfrac{\det \Sigma_Q}{\det \Sigma_P}\right)\Big) \\ &= \tfrac{1}{2}(\boldsymbol{\mu}_Q - \boldsymbol{\mu}_P)^t \Sigma^{-1}(\boldsymbol{\mu}_Q - \boldsymbol{\mu}_P), \end{aligned} \tag{5}$$

where $K = |\boldsymbol{\mu}_P| = |\boldsymbol{\mu}_Q|$ and the second equality holds if the background noise of P and Q is the same, i.e., $\Sigma_P = \Sigma_Q = \Sigma$. It makes this similarity notion symmetrical. Moreover, if the covariance matrix is diagonal constant, i.e., $\Sigma_p(\lambda) = \delta_{g_1,g_1'} \cdots \delta_{g_K,g_K'}\sigma^2$, where $\sigma > 0$, it corresponds to the cost function found in F. A. Dannert et al. (2022). For the sake of consistency, we will use the following notation using J to refer to the KL divergence between two monochromatic photon density distributions with the same covariance matrix Σ,

$$J(P, Q, \Sigma) := 2D_{\mathrm{KL}}\left(\mathcal{N}\left(\sum_{p\in P} \boldsymbol{\mu}_p, \Sigma\right) \| \mathcal{N}\left(\sum_{q\in Q} \boldsymbol{\mu}_q, \Sigma\right)\right), \tag{6}$$

where D_{KL} is multiplied by 2 to have $J(P, \varnothing, \sigma\mathbf{1}) = \mathrm{S/N}(P)^2$, corresponding to the squared expected S/N of configuration P.

A few remarks. First, systematic noise affects data points in a similar manner, causing them to deviate together. However, the cost function takes the difference between signal outputs into account, effectively canceling out the systematic noise component. This allows us to focus on the more meaningful variations and patterns in the output. As a result, this cost function provides a measure of similarity that is robust to systematic noise interference. Second, to gain insight into this concept, consider point P in Figure 4 as the signal generated by P following an observation, e.g., an image with $l = 1.0x_0$ in Figure 3. However, due to background noise, envision a Gaussian distribution in this multidimensional space of images centered around the mean, which is the noiseless image μ_P produced by P. This multivariate Gaussian distribution illustrates the outcomes of observations, factoring in the noise component. As noise decreases or the S/N increases, the Gaussian distribution becomes more localized around μ_P. The quantity $J(P, Q, \Sigma)$ is a proxy for how probable a measure of the output of P would produce the output of Q.

A more general definition of target confusion can be expressed using the principle of parsimony. This principle is also known as Occam's razor. Assume we want to explain the output of P with a model Q_N, which is a configuration of N point sources. Let us add a parsimony cost related to the

model's complexity to select the best model. In our case, the model's complexity is described by the number of point sources N of the model Q_N. The total cost can be written as follows:

$$J_{\rm tot}(P, Q_N, \Sigma) = J(P, Q_N, \Sigma) + \xi(N),$$

where Q_N is a configuration of N point sources and ξ is a parsimony cost related to the model's complexity. If $N > M$, then $\xi(N) > \xi(M)$. This model selection requires that $|Q^\star_{\rm tot}| \leqslant |P|$, where $Q^\star_{\rm tot}$ is the model that minimizes the total cost function $J_{\rm tot}$ with respect to the ground truth P. Note that without loss of generality, we can set $\xi(0) = 0$. In the next two sections, we will study two specific cases where the ground truth is a two-point-source configuration, which means $|P| = 2$.

2.2.3. Criterion for Spectral Contamination

In this section, we study how two point sources can look like one point source that is different from the ones present in the ground truth. Let $|P| = 2$ and assume that the model with a single point source $Q^\star = \text{argmin}_{Q:|Q|=1} J(P, Q)$ minimizes the total cost. It implies that the two following equations must be satisfied:

$$J(P, Q^\star, \Sigma) < \xi(2) - \xi(1) =: \eta^2 \quad \eta > 0, \tag{7}$$

$$J(P, \varnothing, \Sigma) > J(P, Q^\star, \Sigma) + \xi(1) > \xi(1) =: \eta^2_{\rm S/N} \quad \eta_{\rm S/N} > 0. \tag{8}$$

The first equation tells us that $Q^\star$ must have a high enough probability of producing an output similar to P. We notice that given η, if $J(P, Q^\star, \Sigma) \Leftrightarrow 0$, there is always a scaling of the noise $\beta > 0$, $(\Sigma \rightarrow \beta\Sigma)$ such that Equation (7) is not satisfied. It means that there is always an S/N of P such that we can resolve nonoverlapping point sources. The second equation tells us that the S/N of P must be higher than a threshold value. It means that there is no possible contamination if there is no detection. Finally, to have contamination, the model $Q^\star$ must be different enough from existing point sources in the ground-truth P. Indeed, this ensures that the point source described by the simpler model $Q^\star$ does not already exist. For instance, if an observation yields only one detected point source where there are actually two, but the detected point source resembles one of the actual sources, then we have detected something that exists regardless. Hence, we do not consider that as contamination. To have spectral contamination, we impose the following condition:

$$\min_{P_s \in \mathcal{P}(P) - \{P\}} J(P_s, Q^\star, \Sigma) > \alpha\eta^2, \tag{9}$$

where $\mathcal{P}(P) = \{\varnothing, p_1, p_2, P\}$ and $\alpha > 0$ is a constant. The constant α defines how strong we want the latter condition to be. If α is small, then the last condition is weaker; i.e., contamination occurs more frequently.

In summary, for $|P| = 2$, according to Equations (7), (8), and (9), the best single-point-source model $Q^\star$ must satisfy three conditions for contamination to occur:

1. P must be detectable,

$$J(P, \varnothing, \Sigma) > J(P, Q^\star, \Sigma) + \eta^2_{\rm S/N}; \tag{10}$$

2. $Q^\star$ must be indistinguishable from P,

$$J(P, Q^\star, \Sigma) < \eta^2; \text{ and} \tag{11}$$

3. the model $Q^\star$ must be different enough from each existing point source and void,

$$\min_{P_s \in \mathcal{P}(P) - \{P\}} J(P_s, Q^\star, \Sigma) > \alpha\eta^2. \tag{12}$$

Let us define the target confusion map $\mathcal{D}$ of a given configuration with two point sources and background noise covariance matrix Σ as

$$\mathcal{D}(P, \Sigma) = \min_{P_s \in \mathcal{P}(P) - \{P\}} J(P_s, Q^\star, \Sigma) - J(P, Q^\star, \Sigma), \tag{13}$$

where again $Q^\star$ is a single point source that minimizes the cost $J(P, Q)$. The target confusion map is a difference of cost functions and thus is related to a ratio of probabilities. Let $\mathbb{P}_1$ be the likelihood that P can produce the output generated by Q and $\mathbb{P}_2$ be the likelihood that p_1 can produce the output generated by Q. Then, the ratio of probabilities is given by

$$\frac{\mathbb{P}_1}{\mathbb{P}_2} \propto \frac{e^{-J_1}}{e^{-J_2}} = \exp(J_2 - J_1) = \exp(\mathcal{D}), \tag{14}$$

where $J_1 = J(P, Q^\star, \Sigma)$ and $J_2 = J(p_1, Q^\star, \Sigma)$. In the third equality we used, without loss of generality, $J(P_1, Q^\star, \Sigma) = \min_{P_s \in \mathcal{P}(P) - \{P\}} J(P_s, Q^\star)$. Note that $\mathcal{D} = 0$ implies that $\mathbb{P}_1 = \mathbb{P}_2$.

By contrapositive, the contamination criterion is not satisfied if the following condition is satisfied:

$$\mathcal{D}(P, \Sigma) < (\alpha - 1) J(P, Q^\star, \Sigma).$$

First, note that the only value of α that puts a condition on the probability ratio proxy $\mathcal{D}$ independent of P is $\alpha = 1$. Second, if $\xi(2) = 2\xi(1)$, which is the case for the parsimony cost related to the Akaike information criterion (AIC; H. Akaike 1974), then $\eta = \eta_{\rm S/N}$. It means that the cost $J(P, Q^\star, \Sigma)$ must be higher than the detection threshold $\eta^2_{\rm S/N}$ for contamination not to occur. We conclude that two models are indistinguishable if they have a cost less than the detection threshold. Thus, setting $\alpha = 1$ in Equation (9) makes sense because we want $Q^\star$ to be distinguishable from p_1, p_2, or $\varnothing$. These are the reasons why we choose $\alpha = 1$ as a parameter for the condition (Equation (12)). We show in Appendix B what happens if we vary α for traditional telescopes.

In summary, there is no contamination if one of the following conditions is satisfied:

$$P \text{ is undetectable,} \quad \text{S/N}(P, \Sigma) < \eta_{\rm S/N}; \tag{15}$$

$$P \text{ and } Q^\star \text{ are distinguishable,} \quad J(P, Q^\star, \Sigma) > \eta^2_{\rm S/N}; \tag{16}$$

$$\text{target confusion is negative,} \quad \mathcal{D}(P, \Sigma) < 0; \tag{17}$$

where $\text{S/N}(P, \Sigma) = \sqrt{J(P, \varnothing, \Sigma)}$ is the definition of the S/N and $\eta_{\rm S/N} = \sqrt{\xi(1)}$ is the detection threshold. Notice that the sign of the target confusion map is independent from the S/N of P and the detection threshold. It means that its value for a

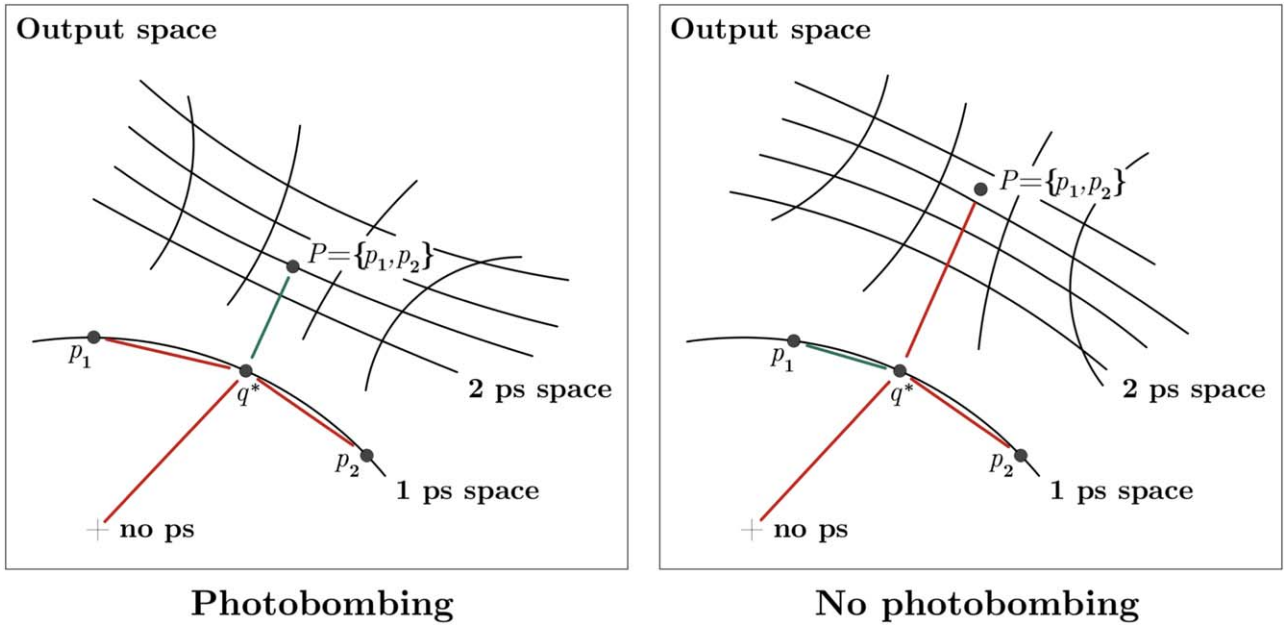

Figure 4. Conceptual examples of photobombing (left) and no photobombing (right) cases. "Output space" represents all images for traditional telescopes or time series for LIFE. "no ps" represents the output when there is no point source, i.e., a black image or flat time series. "1 ps space" represents all noiseless images/time series that one fixed point source can produce. Analogously, "2 ps space" represents all noiseless images/time series that two fixed point sources can produce. $q^\star$ is the one point source that minimizes the loss with P, i.e., P's projection to the generated one point source subspace. In green is the smallest distance of the four distances according to the similarity notion, which is the loss. If the smallest distance, in green, is between P and $q^\star$, then $\mathcal{D} > 0$, and by definition, contamination can occur; otherwise, contamination does not occur. Similar to the Rayleigh criterion, the condition $\mathcal{D} > 0$ is more about the possibility and impossibility of contamination rather than contamination in the absolute sense. Notice that "no ps" $\subset$ "1 ps" $\subset$ "2 ps."

given configuration P depends only on the family of UIRFs defined by the telescope we are observing with.

Similar to what is presented in F. A. Dannert et al. (2022), the detection threshold can be set such that the probability that model selection on noise-only outputs fails to reject $Q_1^\star$ is small enough,

$$\mathbb{P}(\,\mathrm{S/N}\,(Q_1^\star(\boldsymbol{X}),\,\Sigma) > \eta_{\mathrm{S/N}}) = \Phi(5),$$
$$Q_1^\star(\boldsymbol{X}) = \mathrm{argmin}_{Q:|Q|=1}(\boldsymbol{\mu}_Q - \boldsymbol{X})^t\Sigma^{-1}(\boldsymbol{\mu}_Q - \boldsymbol{X}),$$

where $\boldsymbol{X} \propto \mathcal{N}(\boldsymbol{0},\,\Sigma)$ and $\Phi(5) \simeq 1 - 0.9999994$ is the 5σ confidence level. The detection threshold can be approximated using a numerical method that finds $Q^\star$ on a high number of simulated noise-only outputs. In this paper, we focus more on the target confusion map criterion (Equation (24)). Recall that if $\mathcal{D} > 0$, then it is possible but not guaranteed to have contamination. Figure 4 allows us to better see the difference between photobombing (possibility) and nonphotobombing cases via the target confusion map.

A few remarks. First, the condition $J(P,\,Q^\star,\,\Sigma) < \eta^2$, where $\eta > 0$ is a threshold number, is useful for high-S/N scenarios. Specifically, when confronted with a high-S/N image of two point sources, as depicted in Figure 3, we can effectively distinguish the point sources even if they are separated by an angle equal to a fraction of $\delta_{\mathrm{Rayleigh}}$. As said in Section 2.1, in theory, in the limit of high S/N, we can solve both point sources if they do not overlap. Throughout this paper, we refer to contamination/photobombing when $\mathcal{D} > 0$, yet in practice, we are addressing the possibility of contamination, which is similar to the Rayleigh criterion. Second, adding the same point source b to P and $Q^\star$ does not change the cost function. Indeed, b can be considered as systematic noise. Thus, for a configuration P of N point sources, we only need to check spectral contamination for each pair of point sources, which is again similar to the Rayleigh criterion used in P. Saxena (2022). Third, the contamination criterion is based on the hypothesis that point sources do not move during an observation. This can be an issue if the observation time is long compared to the orbital dynamics of the system we observe. It is especially true for low-mass stars. To include moving targets using the same framework, we need to expand the output space to include all outputs that two moving point sources produce. In other words, we need to include all images or time series that two moving point sources can produce. We also need to redefine the model's complexity to use the principle of parsimony and find new algorithms to find $Q^\star$. A first step can be to include all Keplerian moving point sources. This would increase the number of free parameters per point source by four.

2.2.4. Criterion for Canceling Point Sources

In this section, we study how two point sources can cancel each other's signals, whereas they would have been detected if observed independently. Note that cancellation does not affect traditional telescopes. Let $|P| = 2$ and assume that the model with no point source $\varnothing$ minimizes the total cost. It implies that the two following equations must be satisfied:

$$J(P,\,\varnothing,\,\Sigma) < J(P,\,Q^\star,\,\Sigma) + \xi(1), \tag{18}$$

$$J(P,\,\varnothing,\,\Sigma) < \xi(2). \tag{19}$$

Both the first and second equation tell us that the S/N of P must be lower than a threshold value. We notice that there is no cancellation if the S/N of P is over $\xi(2)$. For cancellation to occur, one or both point sources in P must be detectable when observed independently. Thus, we impose the following

condition:

$$\min_{P_s \in \{p_1, p_2\}} J(P_s, \varnothing, \Sigma) < \eta^2_{\mathrm{S/N}}. \tag{20}$$

Similarly to the previous section, we can construct a target cancellation map $\mathcal{C}$, where we assume again that $2\xi(1) = \xi(2)$. Recall that this is the case for the parsimony cost related to AIC and that it implies $\eta = \eta_{\mathrm{S/N}}$. The target cancellation map is defined as follows:

$$\mathcal{C}(P, \Sigma) = \min_{P_s \in \{p_1, p_2\}} J(P_s, \varnothing, \Sigma) - J(P, \varnothing, \Sigma) + J(P, Q^\star, \Sigma). \tag{21}$$

In summary, there is no cancellation if one of the following conditions is satisfied:

$$\text{half } P \text{ is detectable}, \quad \mathrm{S/N}(P, \Sigma)/\sqrt{2} > \eta_{\mathrm{S/N}}; \tag{22}$$

$$\text{both } p_1, p_2 \text{ are undetectable}, \quad \max_{P_s \in \{p_1, p_2\}} \mathrm{S/N}(P_s, \Sigma) < \eta_{\mathrm{S/N}}; \tag{23}$$

$$\text{target cancellation is negative}, \quad \mathcal{C}(P, \Sigma) < 0; \tag{24}$$

where $\mathrm{S/N}(P, \Sigma) = \sqrt{J(P, \varnothing, \Sigma)}$ is the definition of the S/N and $\eta_{\mathrm{S/N}} = \sqrt{\xi(1)}$ is the detection threshold. Notice that the sign of the target cancellation map is independent from the S/N of P and the detection threshold $\eta_{\mathrm{S/N}}$. It means that its value for a given configuration P depends only on the family of UIRFs defined by the telescope we are observing with.

2.2.5. On Multichromatic Distributions

More generally, we can define the multichromatic photon density distribution $\mathcal{N}_p$ of a point source p as

$$\mathcal{N}_p = \mathcal{N}(\boldsymbol{\mu}_p, \Sigma_p),$$

$$\boldsymbol{\mu}_p = \begin{pmatrix} \boldsymbol{\mu}_p(\lambda_1) \\ \vdots \\ \boldsymbol{\mu}_p(\lambda_M) \end{pmatrix},$$

$$\Sigma_p = \Sigma_\lambda \otimes \Sigma_G = \begin{pmatrix} \Sigma_p(\lambda_1) & \Sigma_{p,12} & \dots & \Sigma_{p,1M} \\ \Sigma_{p,21} & \Sigma_p(\lambda_2) & \dots & \Sigma_{p,2M} \\ \vdots & \ddots & \ddots & \vdots \\ \Sigma_{p,M1} & \Sigma_{p,M2} & \dots & \Sigma_p(\lambda_M) \end{pmatrix},$$

where $\otimes$ is the Kronecker product, Σ_λ is the covariance matrix related to different observed wavelengths, and Σ_G is the covariance matrix related to different rotation angles ρ for LIFE or pixels δ_x, δ_y for a traditional telescope. The same reasoning as in the previous section can be applied for multichromatic photon density distributions. If we assume that the covariance matrix Σ_p is diagonal constant by block, which means that there is no correlation between the flux for different wavelengths of observation, then we only have to replace the cost J by the sum of costs over each λ_k factoring in the corresponding noise term $\Sigma(\lambda_k)$. In this paper, we will compute the similarity between multichromatic photon density distributions assuming white Gaussian noise between images of different colors, i.e., diagonal constant by block covariance matrices. Under these restrictions, from Equation (10), we have that if two planets are detectable at λ_1 and λ_2, then they will be detectable at $\{\lambda_1, \lambda_2\}$. Conversely, from Equation (11), if P and $Q^\star$ are indistinguishable at $\{\lambda_1, \lambda_2\}$, then P and $Q^\star$ will be indistinguishable at λ_1 and λ_2. Lastly, for UIRFs that are given by the scaling and translation of some function, e.g., the Airy disk for a circular aperture, Equation (12) holds for $\{\lambda_1, \lambda_2\}$ if it is satisfied for λ_1 and λ_2. Note that every step in Section 2.2.2 can be easily generalized to multichromatic photon density distributions.

2.2.6. δ_0, δ_1, and δ_C Spatial Resolutions

In this section, we introduce a new metric to quantify how prone a telescope is to spectral contamination and cancellation. Let $P = \{p_1, p_2\}$ be the ground truth. The main idea is to fix p_1 at a specific location in the FOV and move p_2 around. We then calculate the surface area within the FOV where the contamination criterion is satisfied, $D(\{p_1, p_2\}) > 0$. This area serves as a measure of how much the telescope is prone to contamination.

First, we define the following indicator function of a two-point-source configuration $P = \{p_1, p_2\}$,

$$\chi(P, \Sigma) = 1_{\mathcal{D}(P,\Sigma)>0}, \tag{25}$$

where χ is the indicator function, which is a unit step function, and Σ is a covariance matrix. The quantity χ is 1 if contamination can occur and 0 if contamination cannot occur. By fixing p_1 and moving p_2 over the FOV, we can quantify the region in the FOV where there is no possible spectral contamination. Formally, we define the resolution map of a point source p_1 with respect to a luminosity flux $\boldsymbol{F}$:

$$\mathcal{R}(p_1, \boldsymbol{F}, \Sigma) = \sqrt{\frac{1}{\pi} \iint_{\mathrm{FOV}} \chi(\{p_1, ((\delta_x, \delta_y), \boldsymbol{F})\}, \Sigma) d\delta_x d\delta_y}. \tag{26}$$

Notice that if the area of contamination is a disk, then $\mathcal{R}$ represents the radius of the disk. We define the δ_1 resolution at point (δ_x, δ_y) for a diagonal constant covariance matrix, i.e., $\Sigma = \sigma \mathbf{1}$,

$$\delta_1(\delta_x, \delta_y, \hat{\Lambda}) = \mathcal{R}(p, F, \sigma \mathbf{1}), \tag{27}$$

where $p = \{\boldsymbol{\theta}_p = (\delta_x, \delta_y), \boldsymbol{F}_p = F\mathbf{1}\}$ is a point source with a constant spectrum for $\lambda \in \hat{\Lambda} = \{\lambda_1, \dots, \lambda_M\}$. Since $H(x) = H(cx)$ for any $c > 0$, we have independence from F and σ. δ_1 is only computed to compare different telescope resolving capabilities in a theoretical scenario. That particular scenario is chosen because δ_1 does not depend on signal amplitude F and the noise σ amplitude. Notice that δ_1 only depends on the telescope's architecture and thus allows for apples-to-apples comparison between telescopes. In practice, to decide if spectral contamination is possible, we check if one of the three conditions (Equations (15), (16), and (24)) is satisfied for a given configuration of point source $P = \{p_1, p_2\}$ representing planets and covariance matrix Σ representing the background noise. A few remarks. First, if $\Sigma = \sigma \mathbf{1}$, then the resolution $\mathcal{R}$ depends on the S/N of p_1 and p_2 via the incoming photon flux F_{p_1} and F_{p_2} and the noise σ. Using the fact that multiplying the flux of p_1 and p_2 by a constant $c > 0$ does not change the resolution, we have that $\mathcal{R}$ only depends on the shape of the UIRF. Second, given p_1 and a background noise covariance

matrix Σ, the function $f(p_2) = \mathcal{D}(\{p_1, p_2\}, \Sigma)$ is bounded by $\mathcal{D}(\{p_1, p_1\}, \Sigma) = J(\{p_1\}, \varnothing, \Sigma)$ and $-J(\{p_1\}, \varnothing, \Sigma)$. Thus, we can normalize the target confusion map as follows:

$$\frac{\mathcal{D}(\{p_1, p_2\}, \Sigma)}{2J(p_1, \varnothing, \Sigma)} + \frac{\mathcal{D}(\{p_1, p_2\}, \Sigma)}{2J(p_2, \varnothing, \Sigma)} \in [-1, 1]. \tag{28}$$

The closer to 1, the harder it is to resolve the point sources. If the value $\mathcal{D}$ is over 0, then it is possible to have spectral contamination. If the value $\mathcal{D}$ is under 0, then there is no spectral contamination. The closer to -1, the easier it is to resolve the point sources. Lastly, δ_1 can be generalized for other parameters than δ_x, δ_y. For example, if we assume Keplerian parameter space for the point sources (six parameters), we can compute the associated δ_1 − resolution.

Similarly, the cancellation map can be normalized as follows:

$$\frac{\mathcal{C}(\{p_1, p_2\}, \Sigma)}{2J(p_1, \varnothing, \Sigma)} + \frac{\mathcal{C}(\{p_1, p_2\}, \Sigma)}{2J(p_2, \varnothing, \Sigma)} \in [-\infty, 1]. \tag{29}$$

We can define a spatial resolution with respect to the target cancellation criterion. Thus, we define the canceling spatial resolution γ using the same construction but replacing the criterion in the indicator function (Equation (25)) with the target canceling criterion $\mathcal{C}(P, \Sigma) > 0$.

Lastly, we define the resolution δ_C associated with the criterion $\mathcal{C} > 0 \cup \mathcal{D} > 0$. Note the surface area in Equation (26) where $\mathcal{D} > 0$ and $\mathcal{C} > 0$ are not necessarily exclusive, meaning that $\delta_1 + \delta_0$ does not equal the resolution obtained with the criterion $\mathcal{C} > 0 \cup \mathcal{D} > 0$. However, we have that

$$\max(\delta_0, \delta_1) \leqslant \delta_C \leqslant \sqrt{\delta_0^2 + \delta_1^2}. \tag{30}$$

2.3. Traditional Telescope's δ_C Resolution

For a traditional telescope, the only geometrical hyperparameter is the diameter d of the aperture. The output parameters are $g_1 = \delta_x$ and $g_2 = \delta_y$, and Γ describes the grid of pixel positions. The unit output functions are given by the Airy disk (Equation (1)) centered at $\boldsymbol{\theta}_p = (\delta_{x,p}, \delta_{y,p})$, and the background noise is assumed to be white noise, i.e.,

$$U_p(\delta_x, \delta_y, \lambda) = \left(\frac{2J_1(\pi\delta_r d/\lambda)}{\pi\delta_r d/\lambda}\right)^2, \tag{31}$$

$$\text{where } \delta_r = \sqrt{(\delta_x - \delta_{x,p})^2 + (\delta_y - \delta_{y,p})^2}, \tag{32}$$

$$\Sigma_p(\lambda) = \delta_{\delta_x,\delta_x'}\delta_{\delta_y,\delta_y'}\sigma_\epsilon^2, \tag{33}$$

where σ_ϵ is the standard deviation of the noise at each pixel position δ_x, δ_y. Thus, to compute the target confusion value $\mathcal{D}$ for monochromatic photon density distributions, we use the following cost function,

$$J(P, Q, \Sigma) = \frac{(\boldsymbol{\mu}_Q - \boldsymbol{\mu}_P)^2}{\sigma^2},$$

where P and Q are configurations of point sources and $\sigma = \sqrt{|\Gamma|\sigma_\epsilon^2}$ is the integrated standard deviation over the grid Γ. We show (Figure 5, left) the target confusion map $\mathcal{D}$ for a traditional telescope. Recall that the region of possible contamination is given by x: $\mathcal{D} > 0$, where x is the distance between the monochromatic point sources. We notice that the resolution is the same for F_{p_1}/F_{p_2} and F_{p_2}/F_{p_1}. This is due to the symmetry of $\mathcal{R}$ coming from U_p (Equation (36)). The cusp at $\approx 0.9\delta_{\text{Rayleigh}}$ comes from the fact that the best single-point-source configuration $Q^\star$ is centered at one of the point sources p_1, p_2 at greater angular separations, and it is centered in between if p_1 and p_2 are close enough. Moreover, we show (Figure 5, right) how the δ_1 resolution changes with the luminosity flux ratio F_{p_1}/F_{p_2}. It seems that two point sources with the same luminosity flux are slightly harder to separate than two point sources with different luminosity fluxes. The δ_1 resolution of a traditional telescope computed numerically is

$$\delta_C(\{\lambda\}) = \delta_1(\{\lambda\}) \approx 0.952 \cdot \delta_{\text{Rayleigh}}(\lambda) \approx 1.16 \cdot \frac{\lambda}{d}, \tag{34}$$

where we used $\delta_0 = 0$ for traditional telescopes, meaning that $\delta_C = \delta_1$. Notice that in this case, δ_1 is independent from (δ_x, δ_y), because U_p has a constant shape for any position of a point source p. We also notice that δ_{Rayleigh} is a close approximation of δ_1. A convergence rate plot (Figure 20) for the δ_1 resolution is presented in Appendix C.

A few remarks. First, the Rayleigh criterion was defined using δ_{Rayleigh}, which was itself arbitrarily defined by the first zero of the Airy disk. The purpose of this angle is not only to compare the spatial resolution capacities of telescopes with each other; i.e., it is not only a standard angle. It is an angle that tells us approximately at what angular separation two point sources can never be confused into only one point source that does not resemble one of the two point sources, regardless of any S/N. Second, δ_1 clearly overestimates contamination because for two point sources where the flux ratio F_{p_1}/F_{p_2} is approaching 0, we still have $\delta_1 > 0$. In these cases, contamination should be negligible. Lastly, $\gamma = 0$ for traditional telescopes. This is because there is no destructive interference in such instruments.

2.4. LIFE and Nulling Baseline Optimization

The double Bracewell beam combination scheme currently considered for LIFE's X-array architecture leads to the following transmission map T (F. A. Dannert et al. 2022):

$$T(\delta_r, \delta_\theta, \lambda) = \sin\left(\frac{\pi b_{\text{null}}}{\lambda}\delta_r \cos(\delta_\theta)\right)^2 \sin\left(\frac{2\pi q b_{\text{null}}}{\lambda}\delta_r \sin(\delta_\theta)\right), \tag{35}$$

where $(\delta_r, \delta_\theta)$ is the apparent position of the planet/point source. We define $\delta_{\text{null}} = \lambda_0/b_{\text{null}}$, where $\lambda_0 = 10\,\mu$m.

For LIFE, the unit output functions are given by time series around its transmission map (Equation (35)), and the background noise is assumed to be white noise, i.e.,

$$U_p(\rho, \lambda) = T(\delta_{r,p}, \delta_{\theta,p} + \rho, \lambda), \tag{36}$$

$$\Sigma_p(\lambda) = \delta_{\rho\rho'}\sigma_\epsilon(\lambda), \tag{37}$$

where ρ is the rotation angle of LIFE, which is the only output parameter, and $\Gamma = \{0, \ldots, 2\pi\}$. σ_ϵ is the standard deviation of the noise at each "pixel" $\rho \in \Gamma$. To gain more insight, for a fixed λ, the output signal is in the form of a time series where "time" is the rotation angle of the array. A point source p with apparent position $\boldsymbol{\theta}_p = (\delta_x, \delta_y) = (\delta_r \cos(\delta_\theta), \delta_r \sin(\delta_\theta))$ and

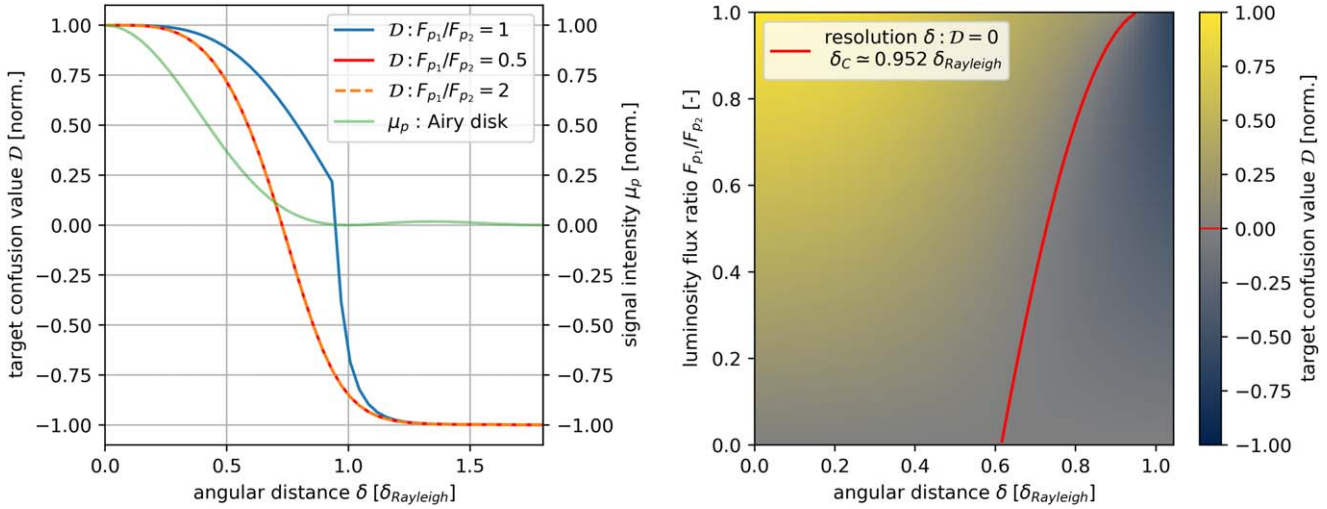

Figure 5. Left: target confusion map $\mathcal{D}(\{p_1, p_2\}, \Sigma)$, where $p_1 = (\boldsymbol{\theta}_{p_1} = (\delta_{x,1} = 0, \delta_{y,1} = 0), \boldsymbol{F}_{p_1} = F_{p_1})$ is a monochromatic point source at a fixed position and $p_2 = (\boldsymbol{\theta}_{p_2} = (\delta_{x,2}, \delta_{y,2}), \boldsymbol{F}_{p_2} = F_{p_2})$ is a monochromatic point source compared to the Airy disk in light green, where $\delta = (\delta_{x,2}^2 + \delta_{y,2}^2)^{1/2}$. Σ is a diagonal constant covariance matrix representing white background noise. When p_1 and p_2 are close, the output from P looks like one point source, i.e., $\mathcal{D} > 0$. When far apart, the output from P does not look like one point source, i.e., $\mathcal{D} < 0$. F_{p_1}/F_{p_2} is the luminosity flux ratio. Right: target confusion map $\mathcal{D}(\{p_1, p_2\}, \Sigma)$ of a configuration of two monochromatic point sources $P = \{p_1, p_2\}$, where $p_1 = (\delta_{x,1} = 0, \delta_{y,1} = 0, \boldsymbol{F}_{p_1})$ is fixed for different luminosity flux ratios. In red is the resolution map $\mathcal{R}(\{p_1\}, F_{p_2})$ for different luminosity flux ratios F_{p_1}/F_{p_2}. At $F_{p_1} = F_{p_2}$, $\mathcal{R} = \delta_1$. Spatial resolution $\delta_1 \approx 0.952\ \delta_{\text{Rayleigh}}$, where δ_{Rayleigh} refers to the classical notion of resolution, i.e., the first zero of the Airy disk. This figure is a generalization of the plot in the left panel.

spectral photon flux $\boldsymbol{F}_{p,\lambda}$ at wavelength λ yields the following time series:

$$\mu_p(\rho) = F_{p,\lambda} T(\delta_{r,p}, \delta_{\theta,p} + \rho, \lambda), \tag{38}$$

where ρ is the angle of rotation of the array. An example with two time series resulting from two planets located at two different positions is shown in Figure 6.

The modulation efficiency (O. P. Lay 2004) is given by

$$\xi(\delta_r) = \sqrt{\int_4^{18.5} \int_0^{2\pi} \mu_p^2(\rho, \lambda) d\rho d\lambda} \tag{39}$$

and quantifies how sensitive the telescope is for a planet that has an angular separation of δ_r from the star. It is related to the cost function $\sqrt{J(P = \{p_1\}, \varnothing, \Sigma = \mathbf{1})}$.

If one does not know the inclination angle of the orbit plane ϕ (by definition face-on $\equiv \phi = 0$), the expected signal intensity over the distribution of inclination angles ϕ and circular orbit trajectory is also useful to know. In that case, the point-source angular separation δ_r is given by

$$\delta_r = \frac{s}{S_{\text{dist}}} \sqrt{\cos^2(\theta) + \sin^2(\theta)\cos^2(\phi)}\,, \tag{40}$$

where s is the semimajor axis and S_{dist} is the observer–star distance. Note that $\phi \propto \arccos(u)$, where $u \in [0, 1]$ is uniformly distributed. By averaging over both ϕ and θ angles and assuming the luminosity flux to be a blackbody radiance spectrum, we can determine the semimajor axis at which the telescope exhibits the highest average sensitivity for a planet of temperature T. We show (Figure 7) the normalized signal intensity for a blackbody radiating point source at Earth's surface temperature $T = 280$ K. For a planet with temperature $T = 280$ K, we find that the planet signal is maximized when $\delta_r = \delta_H \coloneqq 0.91$ □ □$_{\text{null}}$. In our analysis, we will try to set □$_{\text{HZ}}$ = □$_{\text{H}}$ to maximize the planet's signal. This is not always possible, since $b_{\text{im}} < 600$ m. For these cases, we will set $b_{\text{im}} = 600$ m.

2.5. LIFE's δ_0 and δ_1 Spatial Resolutions

The corresponding cost between multichromatic photon density distributions is given by the same cost as found in F. A. Dannert et al. (2022),

$$J(P, Q, \Sigma) = \sum_{\lambda_k} \frac{(\boldsymbol{\mu}_Q(\lambda_k) - \boldsymbol{\mu}_P(\lambda_k))^2}{\sigma(\lambda_k)^2} \Delta\lambda_k,$$

where P and Q are configurations of point sources and $\sigma(\lambda_k) = \sqrt{|\Gamma|\sigma_\epsilon(\lambda_k)}$ is the integrated noise over Γ. In practice, we have access to σ via LIFEsim, which considers all relevant astrophysical noise terms.

We show (Figure 8) the target confusion map $\mathcal{D}$ (Equation (13)) for a configuration of two point sources with one point at a fixed position. We see that there are two regions of interest delimited by the 0 level line in red ($\mathcal{D} = 0$). If p_2 is inside the region $\mathcal{D} > 0$, then photobombing is possible. The resolution $\mathcal{R}$ is defined using the area of this region. If p_1 and p_2 overlap (black dot), the resulting $Q^\star$ is a point source with luminosity flux $\boldsymbol{F}_q = \boldsymbol{F}_{p_1} + \boldsymbol{F}_{p_1}$ located at the same position. If p_2 is at the opposite side and $\boldsymbol{F}_{p_2} < \boldsymbol{F}_{p_1}$, then for all λ, p_2 would cancel the signal from p_1 in a coherent manner. Thus, the resulting $Q^\star$ is a point source with luminosity flux $\boldsymbol{F}_q = \boldsymbol{F}_{p_1} - \boldsymbol{F}_{p_2}$ at p_1's position. Note that these addition and subtraction rules are valid only at two positions, namely, the same for addition and the opposite for subtraction. More generally, if the point source p_2 is in the region $\mathcal{D} > 0$, the resulting S/N of $Q^\star$ would be a more complex combination of p_1's and p_2's spectra. We will provide a concrete example in the study of an Earth twin in Section 3.1.1. Finding $Q^\star$ is key to studying the occurrence of photobombing. Practically, in this paper, this is done using linear regression and Newton–Raphson method techniques alternatively. We use the analytical expression of the transmission map to make faster and more accurate computations.

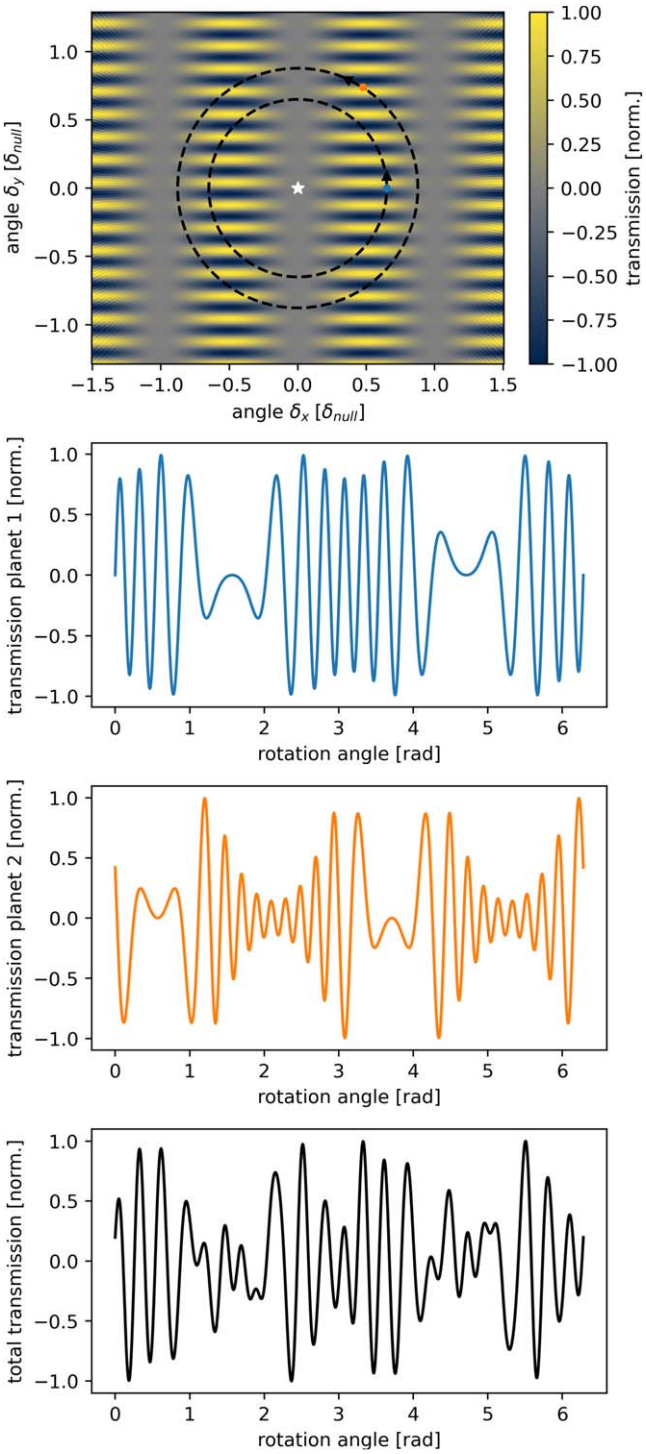

Figure 6. Top: normalized differential transmission map T at $\lambda = \lambda_0 = 10\ \mu$m (Equation (35)) compared to the apparent position of a star at the center and the apparent path of two exoplanets with an apparent angle of $\delta_r = 0.65\delta_{\text{null}}$ and $\delta_r = 0.88\delta_{\text{null}}$ from its star after rotating LIFE about the LIFE–star axis. The second and third plots are the normalized time series of the corresponding planets in the top plot. Bottom: normalized time series of the total signal of the planets in the top plot, where planet 1 (blue) has twice the luminosity of planet 2 (orange) at $\lambda = 10\ \mu$m.

We show (Figure 10, left) the resolution map $\mathcal{R}(p_1, \boldsymbol{F}_{p_2} = F_{p_2}\mathbf{1}, \Sigma = \text{diag}_{\lambda_k \in \hat{\Lambda}}(\Sigma(\lambda_k)))$,where $p_1 = ((\delta_{r,p_1}, 0), \boldsymbol{F}_{p_1} = F_{p_1}\mathbf{1})$ and $\Sigma(\lambda_k)$ is diagonal constant. We see that the resolution is not highly dependent on the luminosity flux ratio F_{p_1}/F_{p_2} and the angular separation $\delta_{r,p}$ for $\delta_{r,p} > 0.15\delta_{\text{null}}$. This map characterizes the performance of the transmission map to resolve two point sources, and it can be compared to resolution maps from other transmission maps. We notice (Figure 10, right) that the δ_1 resolution of LIFE is surprisingly similar to the δ_1 resolution of a large traditional telescope of diameter $d = b_{\text{im}}$ observing at 4 μm. This exactly corresponds to the first approximation made in the Introduction without using this new theoretical framework.

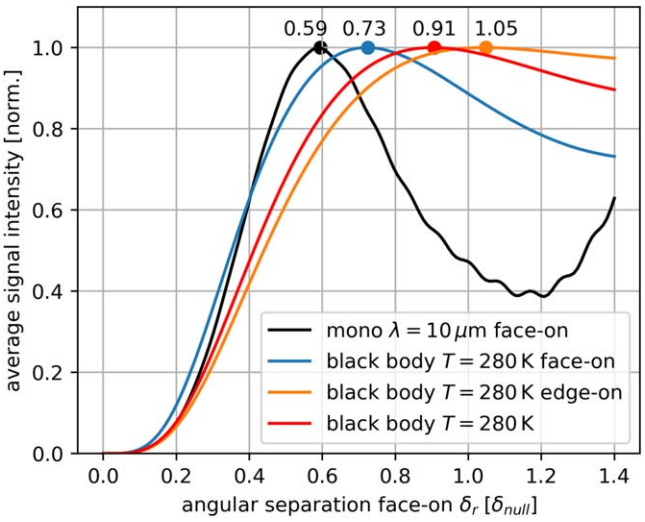

Figure 7. Normalized expected signal intensity for a blackbody radiating point source at temperature 280 K with a maximum semimajor axis angle of δ_r. Black is the signal intensity at $\lambda = 10\ \mu$m and face-on, i.e., $\phi = 0$. Blue is averaged over orbital angle θ face-on. Orange is averaged over orbital angle θ edge-on, i.e., $\phi = \pi/2$ rad. Red is averaged over θ and ϕ. Without any information about ϕ, we set the baseline such that the apparent HZ center radius angle δ_{HZ} matches $0.91 \cdot \delta_{\text{null}}$.

We show (Figure 9) the target cancellation map $\mathcal{C}$ (Equation (13)) for a configuration of two point sources with one point at a fixed position. We see that there are multiple regions of interest delimited by the 0 level line in red ($\mathcal{C} = 0$). If p_2 is inside the region $\mathcal{C} > 0$, then cancellation is possible. The resolution δ_0 is defined using the area of this region. Notice that this is the worst-case scenario, where p_1 and p_2 have the same incoming luminosity flux. When the luminosity fluxes are different, the cancellation disappears almost entirely. Indeed, if $F_1/F_2 = 0.5$, then for p_1 at $\delta_r = 0.6\delta_{\text{null}}$, there is no cancellation at all, i.e., $\mathcal{R} = 0$.

2.6. Detection and Contamination Probabilities

We want to calculate the probability of photobombing for a given planet knowing that it is detected. First, we define a detected planet to be a planet for which the integrated S/N over all wavelengths for 100 hr of integration time is above a threshold $\text{S/N}_{\text{target}} = \eta_{\text{S/N}}$. Thus, the detection indicator function is given by

$$D_p(t) = H(\text{S/N}_{p(t)}(\Lambda) - \text{S}/\text{N}_{\text{target}}), \tag{41}$$

where t represents the time evolution of the system, $p = p(t)$ describes the point source corresponding to the planet, H is the Heaviside function, and $\text{S/N}_{p(t)}(\Lambda)$ is the S/N over the wavelength range $\Lambda = [4\ \mu\text{m}, 18.5\ \mu\text{m}]$ after 100 hr of integration time. This criterion pertains to the intensity of the signal rather than the final S/N. At each time t, we calculate the

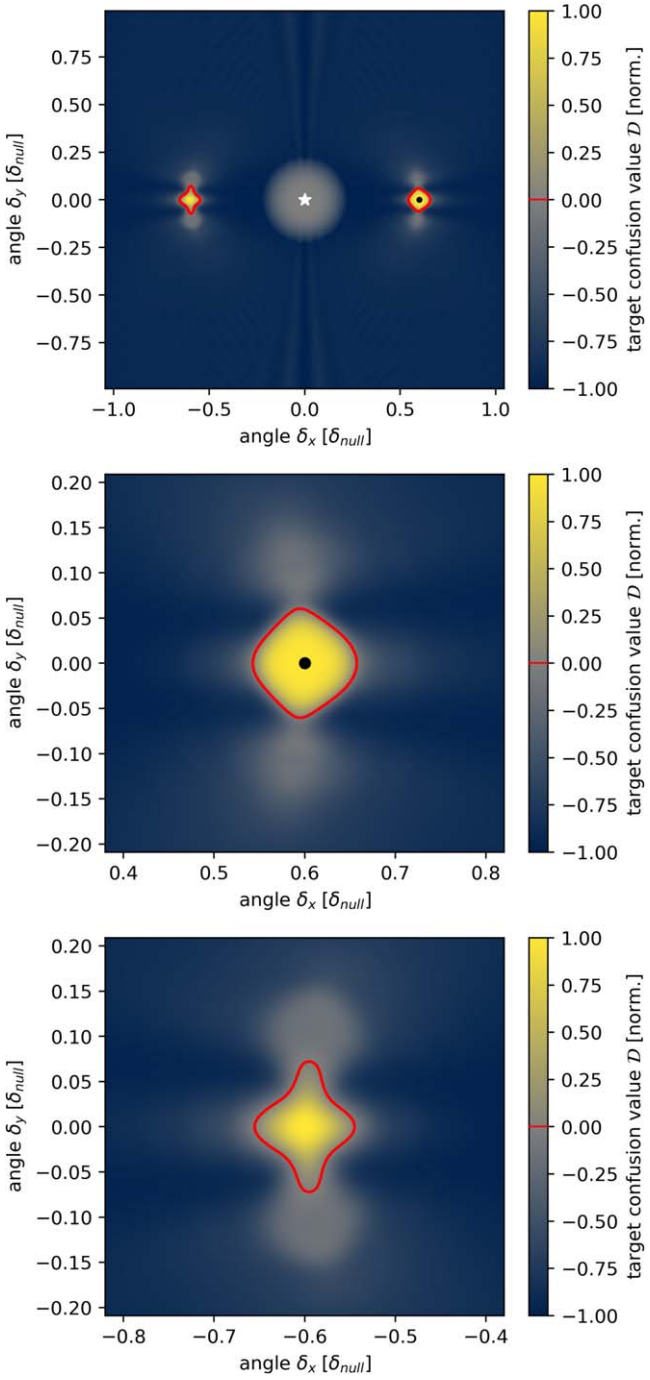

Figure 8. Top: normalized target confusion map $\mathcal{D}$ (Equation (13)) for $p_1 = ((0.6 \cdot \delta_{\text{null}}, 0), \boldsymbol{F}_{p_1})$ (black dot) with homogeneous luminosity flux $\boldsymbol{F}_{p_1} = F_{p_1}\mathbf{1}$ across the full wavelength range, λ from 4 μm to 18.5 μm, and a spectral resolution of 20. At each point where (δ_x, δ_y) is computed, the target confusion map is evaluated at $P = \{p_1, p_2\}$, where $p_2 = ((\delta_x, \delta_y), \boldsymbol{F}_{p_2} = 0.5F_{p_1}\mathbf{1})$ with constant noise independent from P, i.e., $\sigma(\lambda) = \sigma$. When p_2 is outside the red region, photobombing does not occur. The red region is independent from F_{p_1} and σ. In this case, $b_{\text{im}} = 6b_{\text{null}}$ and $\mathcal{R} \approx 0.08\ \delta_{\text{null}}$. Middle: zoom in the region of local photobombing; i.e., two point sources look like one nonexisting point source, and they appear in close proximity. Bottom: zoom in the region of nonlocal photobombing; i.e., two point sources look like one nonexisting point source, and they do not appear in close proximity.

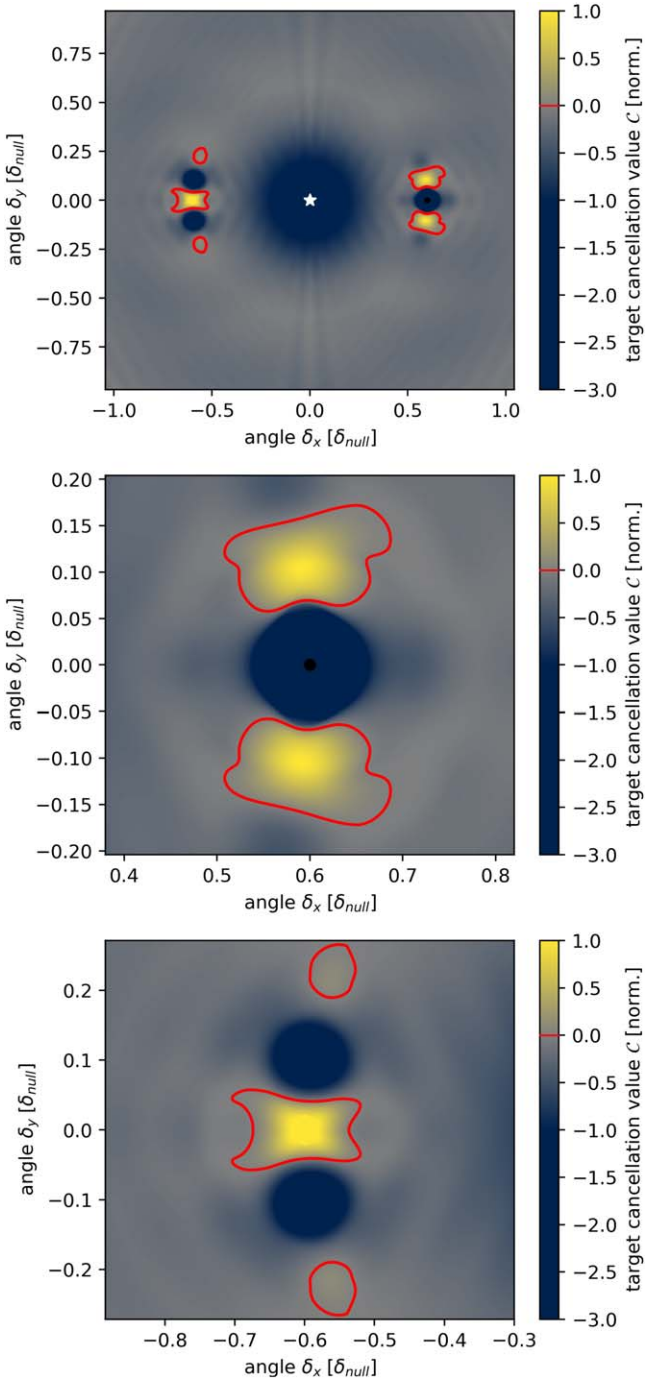

Figure 9. Top: normalized target cancellation map $\mathcal{C}$ (Equation (21)) for $p_1 = ((0.6 \cdot \delta_{\text{null}}, 0), \boldsymbol{F}_{p_1})$ (black dot) with homogeneous luminosity flux $\boldsymbol{F}_{p_1} = F_{p_1}\mathbf{1}$ across the full wavelength range, λ from 4 μm to 18.5 μm, and a spectral resolution of 20. At each point where (δ_x, δ_y) is computed, the target cancellation map is evaluated at $P = \{p_1, p_2\}$, where $p_2 = ((\delta_x, \delta_y), \boldsymbol{F}_{p_2} = F_{p_1}\mathbf{1})$ with constant noise independent from P, i.e., $\sigma(\lambda) = \sigma$. When p_2 is outside the red region, cancellation does not occur. The red region is independent from F_{p_1} and σ. In this case, $b_{\text{im}} = 6b_{\text{null}}$ and $\delta_0 \approx 0.13\ \delta_{\text{null}}$. Middle: zoom in the right region of the top plot. Bottom: zoom in the left region of the top plot.

S/N of the planet as if we were able to integrate for 100 hr, with the planet remaining at a fixed position. According to S. P. Quanz et al. (2022), an integrated S/N of 7 is required for detection.

We define the detection probability of a given planet/point source p as the probability of detection. It is given by

$$\mathbb{P}(D_p = 1) = P_D = \lim_{T\to\infty} \frac{1}{T} \int_0^T D_p(t)dt \tag{42}$$

for short observation times.

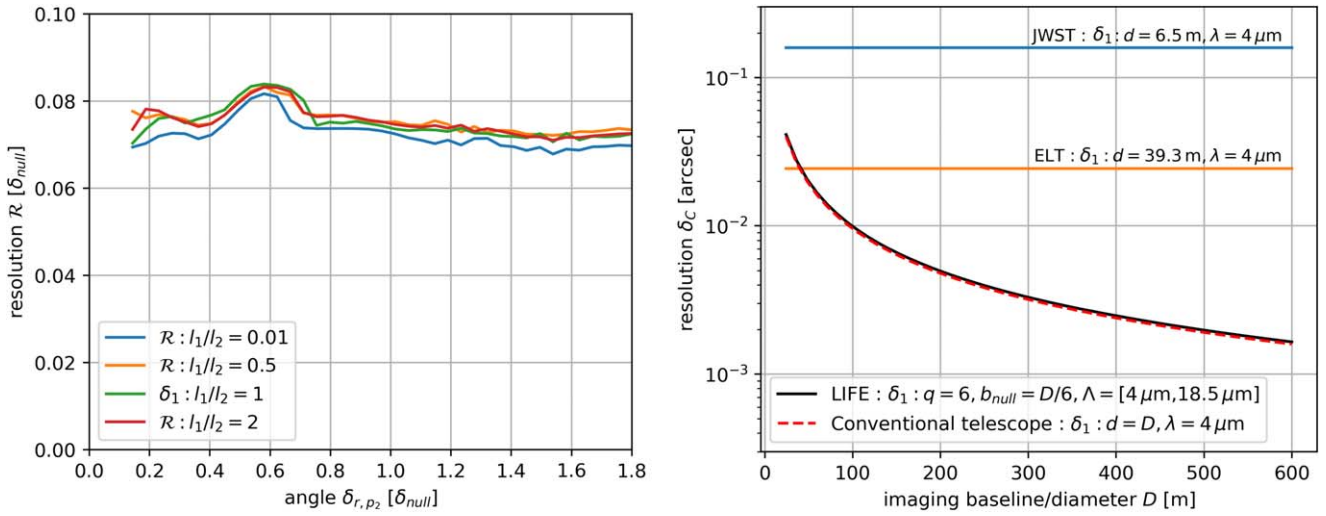

Figure 10. Left: resolution $\mathcal{R}(p_1, \boldsymbol{F}_{p_2} = F_2\mathbf{1}, \sigma(\lambda) = \sigma)$ (Equation (26)) for point sources with homogeneous luminosity fluxes $\boldsymbol{F}_{p_i} = F_{p_i}\mathbf{1}$, $i = 1, 2$. We give the spatial resolution calculated for different angular separation δ_r It corresponds to the length given by the square root of $1/\pi$ of the area of contamination evaluated at $P = \{p_1, p_2\}$ where $\delta_{r,p_1} = \delta_r$ and $\sigma_P = \text{const}$. For example, at an angular separation delta_r = 0.6, and luminosity ratio l_1/l_2=0.5 it corresponds to the angular radius of a disk with the same area than the red area found in . $\mathcal{R}$ weakly depends on the luminosity flux ratio $F_r = F_1/F_2$. Right: comparison between LIFE's δ_1 resolution with JWST and the Extremely Large Telescope. In this case, $b_{\text{im}} = 6b_{\text{null}}$.

We define the contamination indicator function of a point source/planet p by checking if any other planet p_1, p_2, … photobombs planet p. Its indicator function is given by

$$C_{p,P}(t) = H(\max_{i=1,2,\ldots} \mathcal{D}(\{p, p_i\}, \Sigma)), \tag{43}$$

where $P = \{p_1, p_2, \ldots\}$.From that, we define the contamination probability of a given planet/point source p as the probability of contamination, knowing that it is detected. It is given by the following:

$$\mathbb{P}(C_{p,P} = 1 | D_p = 1) = P_C = \lim_{T\to\infty} \frac{\int_0^T C_{p,P}(t) D_p(t) dt}{\int_0^T D_p(t) dt}. \tag{44}$$

In practice, we approximate this quantity using Monte Carlo integration. Assuming circular orbits, we randomize the orbit angle θ of every planet uniformly over $[0, 2\pi]$. For instance, a planet with a detection probability of 80% means that it would be detectable approximately 80% of the time, assuming the planet does not move along its orbit during an observation. Similarly, a contamination probability of 10% means that 10% of the detections are contaminated; i.e., we detect only one planet instead of two planets. Note that the detection and contamination criteria do not take into account moving targets.

The uncorrelation time is defined for a given planet and represents the time it takes for a first observation to become uncorrelated with a second observation, taking into account spectral contamination. We define the probability of having no contamination at time $t + T$ after contamination at time t as $P_2(T)$. The uncorrelation time $T^\star$ is then the smallest time at which $P_2(T^\star) \approx P_C$. When the observation duration becomes comparable to the uncorrelation time, the assumption of static point sources is no longer valid. In such cases, considering the motion of planets during an observation becomes necessary to estimate whether contamination occurs. Unlike the contamination probability, the uncorrelation time captures information about the dynamics of the planets of the system we consider. An example illustrating this concept is presented in Appendix D.

3. Results and Discussion

As mentioned earlier, there are several considerations one must bear in mind. Given two point sources/planets p_1, p_2 in the FOV with respective positions $\boldsymbol{\theta}_{p_1} = (\delta_{x,1}, \delta_{y,1})$, $\boldsymbol{\theta}_{p_2} = (\delta_{x,2}, \delta_{y,2})$ and incoming photon flux $\boldsymbol{F}_{p_1}$, $\boldsymbol{F}_{p_2}$, we can define a configuration $P = \{p_1, p_2\}$.

1. The outputs of a given telescope are modeled as Gaussian multivariate distributions with a mean related to the UIRF and covariance matrix related to the background noise.
2. Photon noise is neglected; i.e., we assume that the pixel size is small compared to the variation of the UIRF.
3. When $\mathcal{D}(P, \Sigma) > 0$, there is a possibility of contamination only. However, when $\mathcal{D}(P, \Sigma) < 0$, there is no possible contamination. $\mathcal{D}$ is a proxy for a probability ratio; see Equation (14) for more details.
4. δ_1 works the same as the Rayleigh criterion δ_{Rayleigh}. First, it overestimates spectral contamination, but δ_1 depends on δ_x, δ_y and the wavelength range Λ. Second, it generalizes to more than two point sources by checking contamination for each pair of point sources.
5. During an observation, all planets are supposed to be at fixed positions. To better assess the potential of contamination in the case of moving targets, it is necessary to augment the space of images/time series generated, reconsider how to apply the parsimony principle, and find other numerical methods to solve the optimization problem of finding $Q^\star$.
6. The contamination probability P_C is defined by the probability that a given detected planet is contaminated, all while considering that the planet does not move during the observation. It is different from the probability of contamination during an observation $P_O(T)$, where time T is the observation time. We always have $P_O > P_C$, and if $T << \text{uncorrelation time}$, we have $P_O \simeq P_C$. Both P_C and P_O are approximated using Monte Carlo integration.

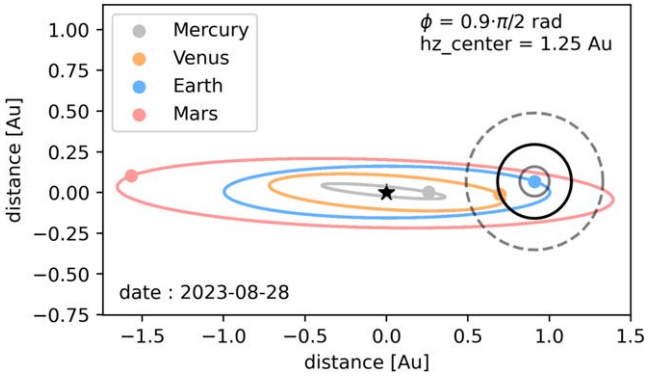

Figure 11. Sun in the center, positions of Mercury, Venus, Earth, and Mars on 2023 August 28 and trajectory of Mercury, Venus, Earth, and Mars from 2020 January 1 to 2030 January 1 viewed from an angle of $\phi \approx 0.9\,\pi/2$ rad from the orbit plane of Earth. Circles represent the resolution of a traditional telescope with diameter $d = b_{\rm im}$. The small one (gray) is for $\lambda = 4$ μm, the medium one (black) is for $\lambda = 10$ μm, and the large one (dashed gray) is for $\lambda = 18.5$ μm. The imaging baseline changes with the star system distance to have optimal sensitivity for planets in the HZ. This representation of the spatial resolution is valid for distances from 6.59 pc (60 m telescope Eq.) up to 65.9 pc (600 m telescope equivalent). Recall that this representation is not an accurate model to decide if photobombing occurs for LIFE.

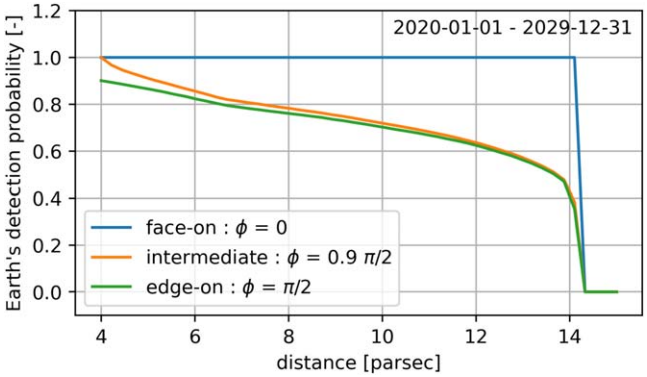

Figure 12. The Earth's detection probability for multiple distances and three different inclination angles of the orbit plane for the period 2020–2030. The detection probability is the probability that the integrated S/N of Earth is above the threshold of 7 after an observation of 100 hr, where we assume that planets do not move. In the face-on case, the angular separation between Earth and the Sun is constant; thus, Earth has the same S/N no matter its location in its orbit. When the system is at a far enough distance, the detection probability drops immediately from 1 to 0 because the S/N will not satisfy the detection criterion for the entire orbit at once.

Table 1
Fixed LIFE Parameters for the Singular Stellar System Studies

Parameter	Value	Description
D	2 m	Aperture diameter
R	20	Spectral resolution
$\eta_{\rm QE}$	0.7	Quantum efficiency
η_t	0.05	Instrument throughput
$S/N_{\rm target}$	7	100 hr S/N detection threshold
$\delta_H/\delta_{\rm null}$	0.91	Apparent HZ center angle
q	6	Scaling factor

3.1. Solar System Analogs

In this section, we will approximate the detection and contamination probabilities using the following LIFE parameters (see Table 1). They are the same as the ones used in F. A. Dannert et al. (2022) for the Earth twin case. The nulling baseline will change according to the apparent HZ center angle and will be in the range of [10 m, 100 m]. Other parameters, such as stellar temperature, planet temperature, level of exozodi emission, etc., will be set by data from each individual system.

3.1.1. Early-type Star System with Long Orbits

Consider the solar system with Mercury, Venus, Earth, and Mars seen from a distance d at an exozodi level of 3. The position of each planet is calculated using Skyfield (B. Rhodes 2019). We show (Figure 11) the apparent positions of orbits for a case between face-on and edge-on. In this case, the orbital plane of Earth is inclined by $\phi \approx 0.9\,\pi/2$ rad. The solar system can be seen with an optimal baseline, i.e., $\delta_{\rm HZ} = \delta_H$, for distances $d \in$ [6.59 pc, 65.9 pc]. The Sun's spectrum is approximated by a blackbody spectrum of temperature $T = 5778$ K. The planet spectra are generated using the Planetary Spectrum Generator developed by G. Villanueva et al. (2018).

We show (Figure 12) the detection probability of Earth for multiple distances using an integrated S/N detection threshold

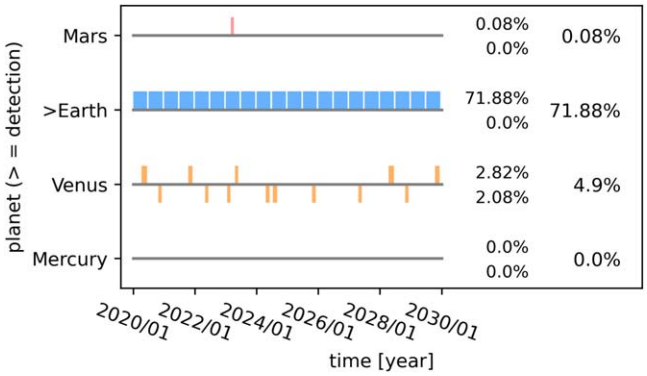

Figure 13. Shown in blue over Earth's gray line is when Earth is detected in a case with $\phi \approx 0.9\pi/2$ rad $\approx 80°$ and a star distance of $d = 10$ pc over the period 2020–2030. The colored bars above the gray lines are indicator functions. When above the gray line, they indicate that, at that time, the planet is contaminating Earth locally. This means that at that moment, the planet and Earth satisfy the contamination criterion $D<0$, appear in close proximity (local contamination), and that Earth is detected (detection is defined in the third line of the above paragraph). However, when the bars are below the gray line, it means that $D<0$ while the planets are not in close proximity (nonlocal contamination) and that Earth is detected. The next two figures show two examples: one with local contamination and one with nonlocal contamination. Mercury does not contaminate Earth's spectrum at any time. Total contamination of 4.98% and a contamination probability of 0.0498/0.7188 ≈ 7%.

of 7 for 100 hr of integration time. We note that for a distance above ∼14 pc, Earth would not be detectable under that criterion. Actually, since the detection criterion is relatively arbitrary, what matters more is how the probability of detection behaves. We understand that in a face-on scenario, the S/N will not depend on the position of Earth along its orbit; thus, when the star distance increases, we get an abrupt decrease in the detection probability. Between 6.59 and 65.9 pc, the nulling baseline can be adjusted to ensure $\delta_H = \delta_{\rm HZ}$, which maximizes the signal for a blackbody spectrum planet at $T = 280$ K orbiting at the center of the HZ. In this particular case, where the system is 10 pc away, we can set the nulling baseline appropriately such that we can ensure that δ_0 matches $\delta_{\rm HZ}$. The slow decrease of the edge-on case comes from the fact that

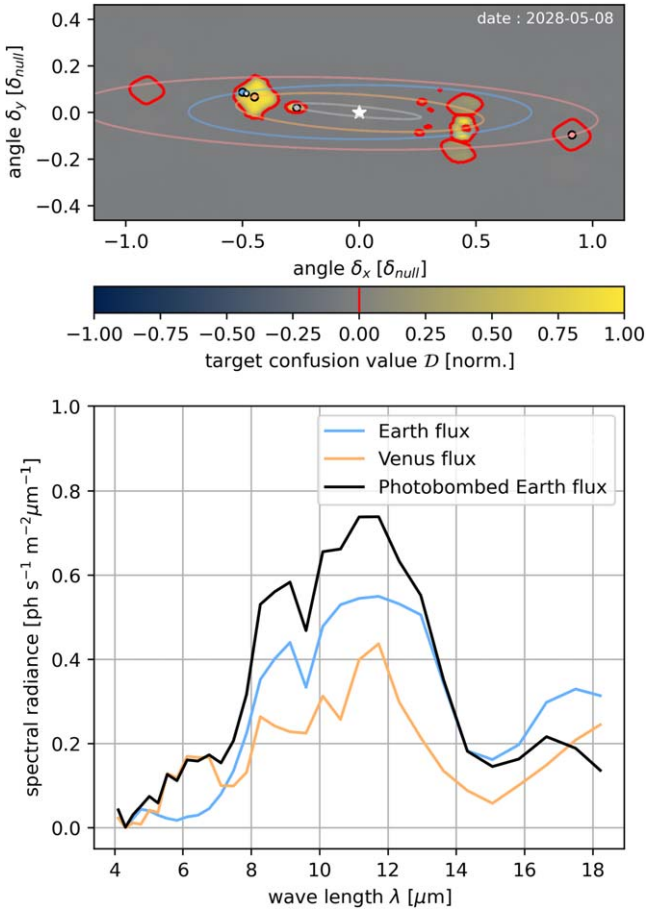

Figure 14. Top: inner solar system seen from a near edge-on angle $\phi \approx 0.9\pi/2$ rad $= 81°$. At each point, $p = (\delta_x, \delta_y)$ is the maximum of the target confusion map between Earth at p and another planet. The red line is $\mathcal{D} = 0$. Earth is inside a region where $\mathcal{D} > 0$; i.e., Earth is photobombed. In this case, Earth is photobombed by Venus. The white dot represents the planet detected in that case. Bottom: flux of Earth, Venus, and the photobombed Earth. Photobombing depends on the flux of both Earth's and Venus's flux. The photobombed Earth's flux is the best point source that generates a signal similar to that of Earth and Venus together.

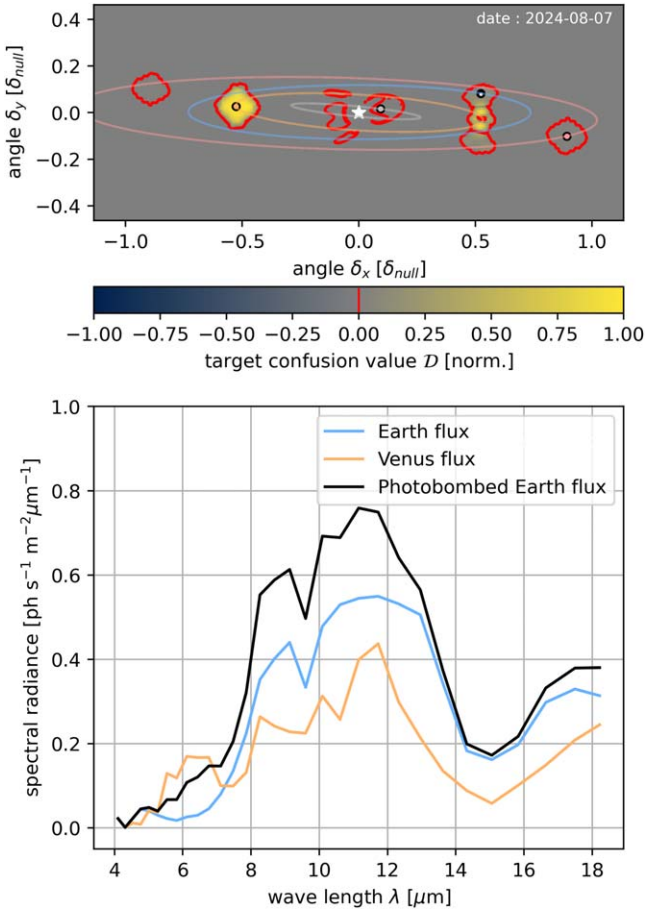

Figure 15. Top: inner solar system seen from a near edge-on angle $\phi \approx 0.9\pi/2$ rad $= 81°$. At each point, $p = (\delta_x, \delta_y)$ is the maximum of the target confusion map between Earth at p and another planet. The red line is $\mathcal{D} = 0$. Earth is inside a region where $\mathcal{D} > 0$; i.e., Earth is photobombed. In this case, Earth is photobombed by Venus nonlocally. The white dot represents the planet detected in that case. Bottom: flux of Earth, Venus, and the photobombed Earth. Photobombing depends on the flux of both Earth's and Venus's flux. The photobombed Earth's flux is the best point source that generates a signal similar to that of Earth and Venus together.

parts of the orbit of Earth are very close to the center of the transmission map, yielding a lower probability of detection.

We show (Figure 13) the detection probability and contamination probability of Earth at 10 pc. The detection probability is approximately 72%. This means that 72% of the time, Earth has a high enough signal intensity, defined by an S/N over 7, for a 100 hr observation, assuming Earth does not move. The contamination probability stands at approximately 7%, indicating that in 7% of detections, Earth has a spectrum contaminated by Venus or Mars. We notice that we recover the detection probability found in Figure 12 at 10 pc with $\phi = 0.9\,\pi/2$ rad. Sometimes Earth gets contaminated by Venus locally (Figure 14), and other times it gets contaminated nonlocally (Figure 15). Local contamination occurs when planets appear in close proximity, while nonlocal contamination arises when planets do not appear close to each other. In the case of LIFE, nonlocal contamination occurs when two planets are positioned on opposite sides. This is due to the symmetry of the transmission map. It is important to note that the photobombed Earth flux is not a simple sum or subtraction of the spectra of Earth and Venus. It is a more complex combination of the two. This is because the transmission map scales with the wavelength. At 10 pc, with $\phi \approx 0.9\pi/2$ rad, the probability that Earth is contaminated during an observation of time $T_{\rm obs} < 100$ hr is close to the value of the contamination probability. This implies that the planets' movement is negligible for observations lasting less than 100 hr.

3.1.2. Lower-mass Star System

In this section, we study the TRAPPIST-1 system, where we assume circular and coplanar orbits. We set the exozodi level to 3 and show (Table 2) relevant data used for the simulation. The planet's temperature allows us to generate a blackbody spectrum for each planet. Contrary to the previous case, we will calculate the detection/contamination probability using Monte Carlo simulations.

Note that in this case the HZ center is relatively small and that we can maximize the expected signal for a blackbody planet of $\delta_H = \delta_{\rm HZ}$ orbiting at the HZ center only if the distance is between 0.188 pc and 1.88 pc. For larger distances, the nulling baseline would be at maximum, i.e., 100 m. We will focus our study on TRAPPIST-1 e, which has the most similar blackbody temperature to Earth.

We show (Figure 16) the detection probability for multiple distances and inclination angles for planet TRAPPIST-1 e. We

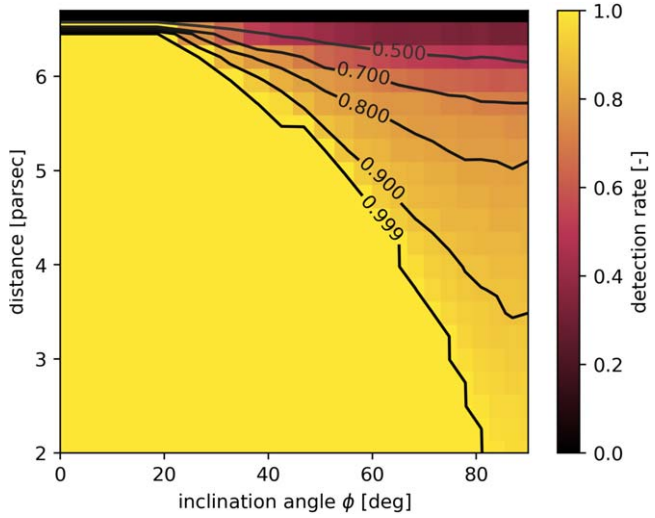

Figure 16. The detection probability of TRAPPIST-1 e. The detection probability is the probability that the integrated S/N of TRAPPIST-1 e is above the threshold of 7 after an observation of 100 hr. TRAPPIST-1 e becomes undetectable for a distance above ≈6.5 pc under that criterion.

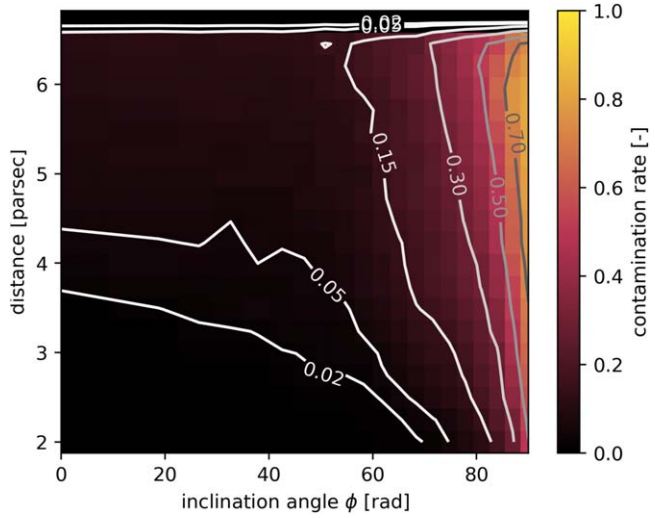

Figure 17. The contamination probability of TRAPPIST-1 e. The contamination probability is the probability that a given detected planet is contaminated. The contamination probability increases with distance and inclination angle.

Table 2
TRAPPIST-1 System Data Input

	Temp. (K)	Radius ($R_\odot$)	HZ Center (mAu)
a	2559	0.12	35.68
	Temp. (K)	Radius ($R_\odot$)	Semimajor (mAu)
b	400.1	1.086	11.11
c	341.9	1.056	15.21
d	288.0	0.772	21.44
e	251.3	0.918	28.17
f	219.0	1.045	37.10
g	198.6	1.127	45.10
h	168.0	0.755	63.00

Note. M. Gillon et al. (2017) contains all necessary features to generate simulations and estimate the contamination probability. More recent papers do not have all the necessary features.

notice the same behavior as Earth for the face-on case ($\phi = 0$), i.e., an abrupt fall of detection probability. Unlike the case of the solar system, at far distances, the limiting factor is not the photon flux or surface area of detection but the nulling baseline, i.e., the size of the interferometer. The decrease in detection probability with the inclination angle is expected. This is because the planet has a higher likelihood of being situated closer to the center of the transmission map, thereby resulting in a weaker signal and lower detection probability.

We show (Figure 17) the contamination probability for multiple distances and inclination angles. Unlike the case of Earth, the contamination probability increases with distance. This is because we are already at the maximum nulling baseline. TRAPPIST-1 e's apparent orbit approaches the center of the transmission map as the distance increases, whereas in the case of the solar system, the Earth remained at the same relative position to the transmission map. We observe that the contamination probability is strongly influenced by the inclination orbit angle, ϕ. Even at identical distances, the contamination probability can vary significantly, ranging from less than 2% to over 70% for a distance of 3.5 pc. Therefore, accurately determining the inclination angle using alternative methods is essential for estimating the extent of contamination.

At 4 pc, $\phi = 0.9\pi/2$ rad. The probability that TRAPPIST-1 e is contaminated during an observation of time $T_{\rm obs} > 48$ hr is close to 1. This occurs because planets move relatively quickly in comparison to the observation time of LIFE. Similar to the previous section, we provide the uncorrelation time, which is approximately 15 hr. This duration is comparable to the typical observation time during the search phase, which lasts from 10 hr up to 100 hr. As mentioned previously, the δ_1 resolution only considers fixed point sources. For these cases, we need to include moving point sources in the theoretical framework to determine whether two moving point sources are entangled or not.

3.2. Population Analysis

The population analysis is done on simulated star systems. The data from S. P. Quanz et al. (2022) contain 500 simulated universes with ≈1700 star systems each, for which there are data about systems we can look at with LIFEsim. The distances range from 1 pc to 20 pc. LIFEsim allows us to calculate the background noise, signal intensity, and planet noise for each planet in each system. We then use that to calculate the target confusion map and decide if contamination occurs. Note that in our study, we have negligible planet noise compared to background noise.

We show (Figure 18) the detection and contamination probabilities of HZ planets for the entire database. About 8% of the HZ planets have a detection probability over >50%. Moreover, we notice that ≈90% are not detectable, meaning that at no point in time will the planet have an integrated S/N over 7 for a 100 hr observation. We show (Table 3) the average number of HZ planets with a detection probability >0%. These are referred to as detectable planets. We show the number of HZ planets with a contamination probability >0%. They represent ≈30% of the detectable planets. We show the number of habitable planets with contamination >5%. They represent

Table 3 Detection and Contamination Probabilities of HZ Planets

Star Type	M	K	G	F
# = average number of HZ planets	853 ± 29	115 ± 11	20.9 ± 4.5	3.8 ± 1.8
# detection probability > 0%	78.1 ± 8.3	10.1 ± 3.0	2.5 ± 1.7	0.8 ± 0.9
# detection probability > 50%	66.5 ± 7.7	9.2 ± 2.9	2.2 ± 1.6	0.8 ± 0.8
# detection probability > 50% and contamination probability > 0%	24.3 ± 5.0	2.7 ± 1.7	0.7 ± 0.9	0.3 ± 0.5
# detection probability > 50% and contamination probability > 5%	12.3 ± 3.8	1.2 ± 1.1	0.3 ± 0.6	0.1 ± 0.3

Note. The average number of habitable planets over universe samples (500 universes of ≈1700 stars each) and average number of HZ planets satisfying conditions on the detection probability and contamination probability. The detection criterion is to have, for a given habitable planet, an integrated S/N over the wavelength range $\Lambda = [4\ \mu\text{m}, 18.5\ \mu\text{m}]$ over $\text{S/N}_{\text{target}} = 7$ for an integration time of 100 hr while assuming that the planets do not move during an observation. The detection probability is the probability of detection of a given habitable planet. The contamination probability is the probability that a given detected habitable planet is contaminated. The error is 1 standard deviation over universe samples.

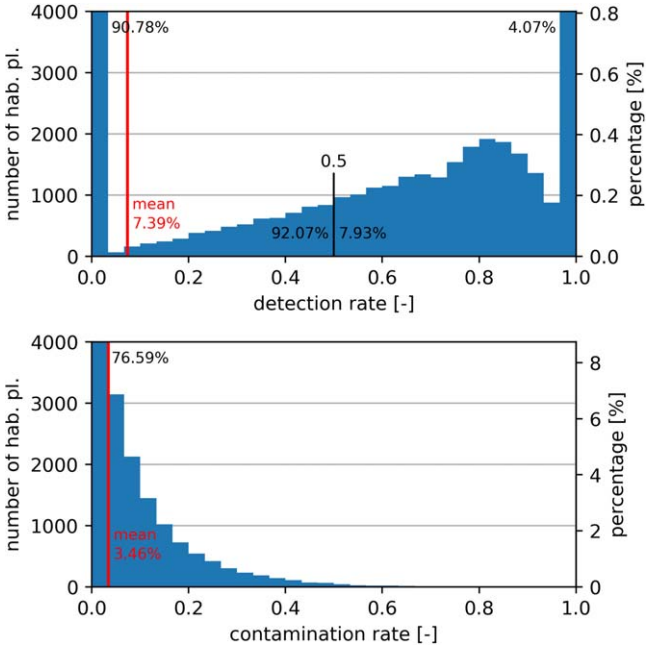

Figure 18. Top: the detection probability for habitable planets for the entire LIFEsim survey (500 universes, ≈1700 systems each). The detection probability is the probability that a habitable planet has an S/N over 7 after 100 hr of observation, while assuming that the planet does not move during the observation. To better see the distribution, the left and right bars are cut off. They represent, respectively, 90.78% and 4.07% of the planets. A total of 7.93% of the planets have a detection rate over 50%. Bottom: the contamination probability for detectable habitable planets, i.e., detection probability >0%. The contamination probability is the probability of a detected planet being contaminated by another planet in the same system. Similarly, the first bar is cut off and represents 76.59% of cases.

approximately 15% of the detectable planets. Lastly, considering that we observe each system for 100 hr, the expected number of detected habitable planets per universe is 73.4 (detected : $\text{S/N}_{\text{target}} > 7$), and the expected number of detected and potentially contaminated habitable planets per universe is 2.1. Thus, less than 2.8% of the habitable planet detections have a contaminated spectrum. We remind the reader that the target confusion criterion overestimates contamination.

4. Summary and Conclusions

This paper provides an approximate upper bound of the spectral contamination occurrence of HZ planets by other planets in the same star system for LIFE. This is done by using the target confusion criterion described in Section 2.2.3. This notion is similar to how the Rayleigh criterion provides a higher estimate for contamination in traditional telescopes. However, this concept can take into account the telescope's output as a whole, i.e., considering all observed wavelengths at once. For instance, LIFE offers the advantage of achieving a spatial δ_1 resolution across its full wavelength range comparable to that of a very large traditional telescope of diameter $D = b_{\text{im}} = 6b_{\text{null}}$ observing at 4 μm, all while utilizing only four relatively small collector spacecraft. However, in the double Bracewell architecture, this benefit comes with trade-offs: first, we can observe only one system at a time; second, there is nonlocal contamination, meaning that two planets may appear as one even if they are not in close proximity; and third, cancellation of point sources can occur, meaning that two point sources can cancel each other's signal while being detectable independently. Nonlocal contamination arises from the anti-symmetric nature of LIFE's transmission map. Cancellation occurs due to the destructive interference of signals in an interferometer.

In the detection phase, LIFE will perform a survey of nearby stars in search of habitable and potentially inhabited planets. These observations need typical timescales of tens of hours. For the actual characterization phase of LIFE, the timescales of observations are even longer. From E. Alei et al. (2022) and B. S. Konrad et al. (2022), we learned that the characterization of Earth twins at 10 pc will take on the order of 50–100 days, while, for example, D. Angerhausen et al. (2023) showed that the detection of potentially biogenic gases in the atmosphere of later-type systems will take on the order of tens of days for targets at typical distances of around 5 pc. The target confusion criterion used in this paper assumes that planets do not move during an observation, again similar to how the Rayleigh criterion works. Incorporating moving point sources would further complicate the theoretical framework by expanding the space of possible signals that moving planets can produce. Thus, this criterion to decide if contamination occurs is accurate when the uncorrelation time is much greater than the observation time. This is the case only for early-type stars and observations that are shorter than 100 hr, which is typical during the search phase.

To summarize, lower-mass stars like TRAPPIST-1 illustrate a resolution limitation in LIFE, leading a priori to more frequent contamination. This limitation arises because the nulling baseline cannot satisfy optimal signal intensity conditions, i.e., $\delta_H = \delta_{\text{HZ}}$. For star distances greater than 2 pc, the nulling baseline would be fixed at its maximum value of 100 m, bringing the apparent HZ closer to the center of the transmission map. Conversely, early-type stars like the Sun

highlight a sensitivity limitation. While the nulling baseline may be optimal for larger distances, there comes a point where, for instance, Earth would no longer be detectable. In this case, the contamination probability does not vary significantly with star distance because the HZ would scale with the transmission map. In both extreme scenarios, the contamination probability is significantly influenced by the orbital inclination angle and the number of planets. For example, for TRAPPIST-1 at $\sim$3.5 pc, the contamination probability can range from under 2% in the best case (face-on) to more than 70% in the worst case (edge-on). For Earth, almost all contamination comes from Venus. In the simulation, Venus is responsible for approximately 98% of the contamination of Earth. We saw in the inner solar system example that LIFE can be prone to nonlocal contamination, i.e., where planets with diametrically opposite positions in the FOV can appear as one planet. Moreover, we saw in that example that this "one planet" has a spectrum that is not a simple linear combination of the spectra of Earth and Venus but a more complex combination of the two. The population analysis based on the search campaign simulations carried out by S. P. Quanz et al. (2022) showed that only 71.3 out of 73.4 detected HZ planets are not contaminated, on average. Hence, this study shows that spectral contamination is not a severe problem for LIFE. The simulations showed that, after all, the increase in spectral contamination for M-type star systems is not significant compared to G-type star systems. We note that this study does not account for other nonplanet sources, such as zodiacal clouds, which can resemble planets and contaminate the signal, occurring a priori more frequently in edge-on cases. One approach to addressing this could be incorporating them into higher-fidelity simulations. This issue must be considered to better quantify the frequency and extent of spectral contamination.

A potential solution to mitigate contamination when the observation time is short compared to the uncorrelation time may be to observe multiple times and wait between observations for the system to uncorrelate, i.e., to not look the same. This will increase the chance of having at least one noncontaminated sample. However, when the observation time is comparable to or longer than the uncorrelation time, this technique may not be effective anymore because the signal would not necessarily be contaminated or noncontaminated during the entire observation window. In that case, we can only integrate the incoming signal until we are confident enough about the configuration of planets in the system. This amounts to relying on the second condition (Equation (11)), i.e., having a sufficiently high S/N, to reduce the probability that one virtual planet can produce the images/time series produced by two planets. To decide if contamination occurs for longer observations, it is necessary to extend the theoretical framework to accommodate moving targets by expanding the space of images/time series to include those produced by two moving point sources and reconsider the application of the parsimony principle, thus finding the best configuration of moving point sources in the much larger space of images/time series. This optimization problem may require different techniques than those used in this paper. Assuming Keplerian dynamics, as done in H. Le Coroller et al. (2020), or having additional information about the system from other observation sites can help solve the optimization problem more efficiently. Another potential way to mitigate spectral contamination is to set up different combination schemes to reduce or eliminate degeneracies, such as nonlocal contamination.

Lastly, the new criteria for contamination and cancellation may also be used in studies investigating different beam combination schemes and mission architectures (J. T. Hansen et al. 2022). Indeed, one could envision finding the best transmission map in a given transmission map space to minimize the resolution δ_1 or the average number of contaminated planets for a given star population. That is not the sole measure, but it can help guide us toward better nulling interferometer architectures.

Acknowledgments

The material is based upon work supported by NASA under award number 80GSFC24M0006. The authors also acknowledge support from the Goddard Space Flight Center (GSFC) Sellers Exoplanet Environments Collaboration (SEEC), which is supported by the NASA Planetary Science Division's Research Program. D.A.'s work has been carried out within the framework of the National Centre of Competence in Research PlanetS supported by the Swiss National Science Foundation under grants 51NF40_182901 and 51NF40_205606. This work has received funding from the Research Foundation - Flanders (FWO) under the grant number 1234224N.

Software: LIFEsim (F. A. Dannert et al. 2022), PSG (G. Villanueva et al. 2018), Sympy (A. Meurer et al. 2017), Skyfield (B. Rhodes 2019).

Appendix A
Numerical Method

In the generalization of spatial resolution, we must find a configuration Q containing a single point source that exhibits a photon density distribution most similar to that of configuration P containing two point sources. This result will allow us to compute the target confusion $\mathcal{D}(P, \Sigma)$. The method has to find the angular position $\boldsymbol{\theta}$ and the flux $\boldsymbol{F}$. We update these parameters via the Newton–Raphson method. The gradient and the Hessian are given by the following:

$$\begin{aligned}
\nabla_{\boldsymbol{\theta},i} &:= 2(\boldsymbol{\mu} - \boldsymbol{d})^t \Sigma^{-1} \partial_i \boldsymbol{\mu} \\
&= 2 \text{ sum } ((\Sigma_F^{-t} M_{\boldsymbol{\mu}-\boldsymbol{d}}^t \Sigma_G^{-1})^t \circ M_{\partial_i \boldsymbol{\mu}}), \\
H_{\boldsymbol{\theta},ij} &:= 2(\partial_i \boldsymbol{\mu}^t \Sigma^{-1} \partial_j \boldsymbol{\mu} + (\boldsymbol{\mu} - \boldsymbol{d})^t \Sigma^{-1} \partial_i \partial_j \boldsymbol{\mu}) \\
&= 2 \text{ sum } (M_{\partial_i \boldsymbol{\mu}^t} \circ (\Sigma_G^{-1} M_{\partial_j \boldsymbol{\mu}} \Sigma_F^{-t}) + (\Sigma_F^{-t} M_{\boldsymbol{\mu}-\boldsymbol{d}}^t \Sigma_G^{-1})^t \circ M_{\partial_i \partial_j \boldsymbol{\mu}}) \\
\theta &\leftarrow \theta - H_{\boldsymbol{\theta}}^{-1} \nabla_{\boldsymbol{\theta}},
\end{aligned}$$

where $\boldsymbol{\mu} = \text{vec}(M_{\boldsymbol{\mu}})$, $\circ$ is the Hadamard product, and sum is the element wise sum. The fluxes F are updated via linear regression. It is an approximation from using Newton–Raphson on all the parameters, i.e., $\boldsymbol{\theta}$ and $\boldsymbol{F}$.

Remark. With this method, the global minimum $Q^\star$ is not guaranteed; however, we can assume that when p_1 and p_2 are about to contaminate each other, the solution $Q^\star$ will be in the neighborhood of one of them. This comes from the smoothness of the cost function with respect to the position of each p_1 and p_2 and the fact that we are interested when the total signal looks like the signal of a single point source.

Appendix B
Varying α for a Traditional Telescope

We show (Figure 19) how the condition (Equation (12)) is satisfied for different values of α. We see that the greater α is, the weaker the contamination criterion becomes. In the paper, we choose $\alpha = 1$.

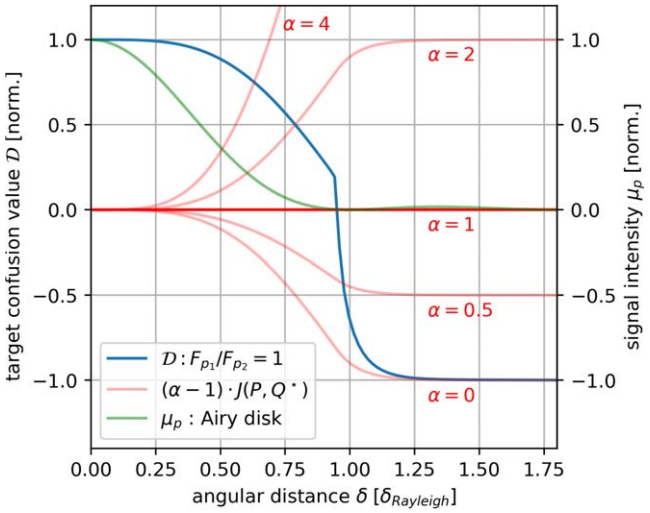

Figure 19. Target confusion value $\mathcal{D}$ (blue) compared to the right-hand side term in Equation (12) (red) for different values of α. If $\mathcal{D}(P, \Sigma) < (\alpha - 1)J(P, Q^\star, \Sigma)$, then by definition of α, there is no contamination.

Appendix C
Convergence Rate of δ_1 Resolution Study

We show (Figure 20) the convergence rate of the δ_1 resolution of traditional telescopes using the numerical method described in Section 2.6. Since there is no known analytical solution, we compared δ_1 to the solution found for a higher number of iterations, here 11. We see that the convergence rate is at least exponential.

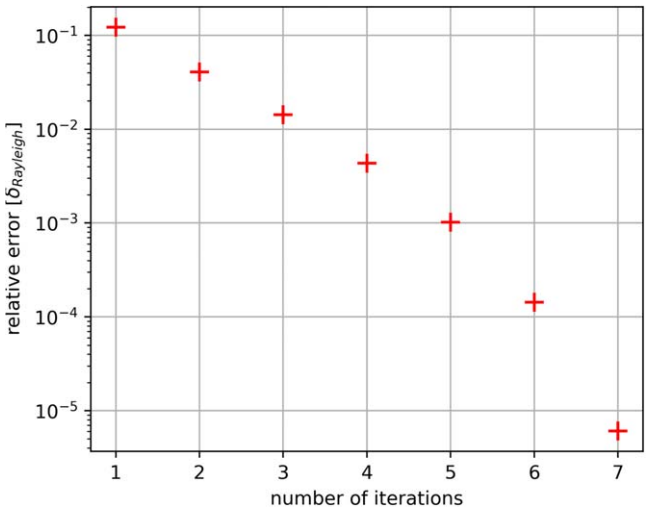

Figure 20. Error $\delta_1(\{\lambda\}) - \delta_{C,11}$ in the number of iterations, where $\delta_{C,11}$ is $\delta_1(\{\lambda\})$ computed at 11 iterations. One iteration corresponds to steps 2 and 3 in the numerical method described in Section 2.6.

Appendix D
Uncorrelation Time Example

In this section, we show how the uncorrelation time is deduced. Given a time series of the contamination indicator function of a planet within a configuration of planets, we can calculate the probability $P_2(T)$ of having no contamination at time $t + T$ after contamination at time t, using Monte Carlo integration techniques. We show (Figure 21) the probability for the case of TRAPPIST-1 e in the TRAPPIST-1 system.

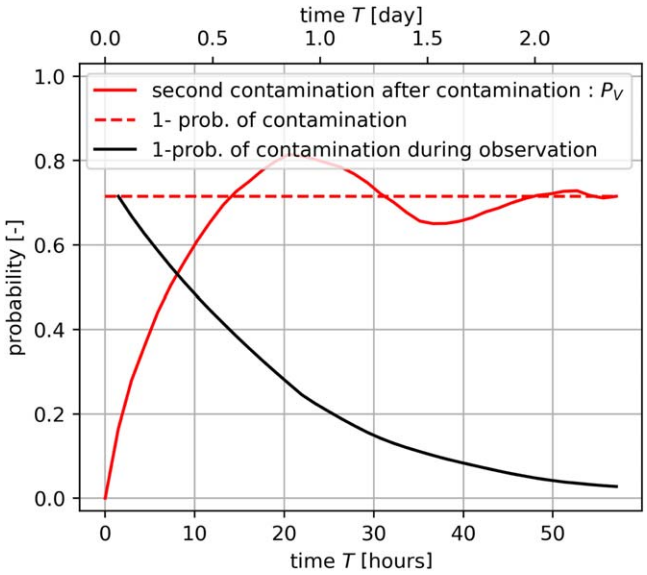

Figure 21. In red is the probability $1 - P_2(T)$ to have contamination at time $t + T$ after having contamination on the first visit at time t for TRAPPIST-1 e. Dashed red is $1 - P_C$, where P_C is the contamination probability of TRAPPIST-1 e. In black is the probability $1 - P_O(T)$ of no contamination during an observation of time T. We read that the uncorrelation time is 15 hr. We notice that $1 - P_O(T > 2 \text{ days}) \approx 0$. Hence, in this case, considering that the system does not change for observations, >15 hr is a bad approximation.

Appendix E
Variables Index

In this section, we provide a table (Table 4) with the description of the symbols used in this paper.

Table 4
Index of Symbols Used in This Paper

Symbol	Description
δ	Apparent angle
S_{dist}	Star distance
r	Apparent distance, $r = \delta \cdot S_{\text{dist}}$
λ	Wavelength
Λ	Wavelength range, $\Lambda = [4\ \mu\text{m}, 18.5\ \mu\text{m}]$
ϕ	Orbit plane inclination (face-on $\phi = 0$ rad, edge-on $\phi = \pi/2$ rad)
θ	Orbit angle (right side $\theta = 0$), used when orbit is assumed to be circular
b_{null}	Null baseline, ranges from 10 m to 100 m for LIFE
q	Scaling factor, $q = 6$ for LIFE
T	Transmission map
S	Sensitivity map
$p = (\delta_x, \delta_y, l)$	Point source at (δ_x, δ_y) with incoming luminosity flux l
U_p	UIRF, function that describes the noiseless output signal of a given point source p with unit flux luminosity in the FOV, same as the PSF idea. In this paper, it can be an image or a time series.
μ_p	Function that describes the noiseless output signal of a given point source p in the FOV. In this paper, it can be an image or a time series.
σ	Total noise term (photon noise = Poisson noise $\approx$ Gaussian noise) coming from background noise σ_b (stellar leakage, local zodiacal dust, exozodiacal dust) and planet noise σ
$P = \{p_1, \ldots, p_N\}$	Set or configuration of point sources
$J(P, Q, \Sigma)$	Cost function between time series of two configurations of point sources P, Q with background noise Σ
$\mathcal{D}(P, \Sigma)$	Target confusion map; if $\mathcal{D} < 0$, then there is no possible contamination
$\mathcal{C}(P, \Sigma)$	Target cancellation map; if $\mathcal{C} < 0$, then there is no possible cancellation
$\mathcal{R}(p_1, \boldsymbol{F}_{p_2}, \Sigma)$	Resolution map: fix one point source and move around the other. This is the area of the positions of p_2 where a given criterion is satisfied. $\mathcal{D}(\{p_1, p_2\}, \Sigma) > 0$ for contamination and $\mathcal{C}(\{p_1, p_2\}, \Sigma) > 0$ for cancellation.
δ_0, δ_1, δ_C	Generalized spatial resolution for the criteria $\mathcal{D} > 0$, $\mathcal{C} > 0$, and $\mathcal{D} > 0 \cup \mathcal{C} > 0$, respectively. Equals $\mathcal{R}$ for the case where $\boldsymbol{F}_{p_1} = \boldsymbol{F}_{p_2} = F\boldsymbol{1}$ for $F > 0$ and $\Sigma = \sigma\boldsymbol{1}$ for $\sigma > 0$.
$D_p(t)$	Detection indicator function; it is 1 if the S/N of 7 is reached in less than 100 hr, assuming the planet stays at a fixed position
$C_{p,P}(t)$	Contamination indicator function, detection and contamination criterion $\mathcal{D}(P, \Sigma) > 0$ satisfied
P_D	Detection probability, probability that a given planet is detected
P_C	Contamination probability, probability that a given detected planet is contaminated
$T^\star$	Uncorrelation time, smallest time between two observations to have uncorrelated contamination occurrence

ORCID iDs

Daniel Angerhausen https://orcid.org/0000-0001-6138-8633
Sascha P. Quanz https://orcid.org/0000-0003-3829-7412

References

Akaike, H. 1974, ITAC, 19, 716
Alei, E., Konrad, B. S., Angerhausen, D., et al. 2022, A&A, 665, A106
Angerhausen, D., Ottiger, M., Dannert, F., et al. 2023, AsBio, 23, 183
Dannert, F. A., Ottiger, M., Quanz, S. P., et al. 2022, A&A, 664, A22
Gillon, M., Triaud, A. H. M. J., Demory, B.-O., et al. 2017, Natur, 542, 456
Hansen, J. T., Michael, J. I. & The LIFE Collaboration 2022, A&A, 664, A52
Konrad, B. S., Alei, E., Quanz, S. P., et al. 2022, A&A, 664, A23
Kullback, S. 1997, Information Theory and Statistics, A Wiley Publication in Mathematical Statistics (New York: Dover Publications) https://books.google.com/books?id=05LwShwkhFYC
Lay, O. P. 2004, ApOpt, 43, 6100
Le Coroller, H., Nowak, M., Delorme, P., et al. 2020, A&A, 639, A113
Meurer, A., Smith, C. P., Paprocki, M., et al. 2017, PeerJ Comput. Sci., 3, e103
Pardo, L. 2018, Statistical Inference Based on Divergence Measures, Statistics: A Series of Textbooks and Monographs (Boca Raton, FL: CRC Press) https://books.google.com/books?id=ziDGGIkhqlMC
Quanz, S. P., Ottiger, M., Fontanet, E., et al. 2022, A&A, 664, A21
Rayleigh, F. R. S. 1879, Philos. Mag. & J. Sci., 8, 261
Rhodes, B., 2019 Skyfield: High Precision Research-grade Positions for Planets and Earth Satellites Generator, Astrophysics Source Code Library, ascl:1907.024
Saxena, P. 2022, ApJL, 934, L32
Villanueva, G., Smith, M., Protopapa, S., Faggi, S., & Mandell, A. 2018, JQSRT, 217, 86